AGU100 ADVANCING EARTH AND SPACE SCIENCE

JGR Solid Earth

RESEARCH ARTICLE
10.1029/2019JB017823

Key Points:
- The strongest variability in East Antarctic lithosphere is observed across Dronning Maud Land and Enderby-Kemp Land
- A slow anomaly extends from the Balleny Islands through the western Ross Embayment, delineating areas of Cenozoic extension and volcanism
- Slow anomalies imaged beneath Marie Byrd Land, the Amundsen Sea Coast, and the Antarctic Peninsula reflect hotspot and subduction processes

Supporting Information:
- Supporting Information S1
- Table S1

Correspondence to:
A. J. Lloyd,
a.j.lloyd@go.wustl.edu

Citation:
Lloyd, A. J., Wiens, D. A., Zhu, H., Tromp, J., Nyblade, A. A., Aster, R. C., et al (2019). Seismic structure of the antarctic upper mantle imaged with adjoint tomography. *Journal of Geophysical Research: Solid Earth*, *124*. https://doi.org/10.1029/2019JB017823

Received 9 APR 2019
Accepted 17 OCT 2019
Accepted article online 25 OCT 2019

Seismic Structure of the Antarctic Upper Mantle Imaged with Adjoint Tomography

A. J. Lloyd[1], D. A. Wiens[1], H. Zhu[2], J. Tromp[3], A. A. Nyblade[4], R. C. Aster[5], S. E. Hansen[6], I. W. D. Dalziel[7], T.J. Wilson[8], E. R. Ivins[9], and J. P. O'Donnell[10]

[1]Department of Earth and Planetary Sciences, Washington University, St. Louis, MO, USA, [2]Department of Geosciences, The University of Texas at Dallas, Richardson, TX, USA, [3]Department of Geosciences and Program in Applied and Computational Mathematics, Princeton University, Princeton, NJ, USA, [4]Department of Geosciences, Pennsylvania State University, PA, USA, [5]Department of Geosciences, Colorado State University, Fort Collins, CO, USA, [6]Department of Geological Sciences, The University of Alabama, Tuscaloosa, AL, USA, [7]Institute for Geophysics, Jackson School of Geosciences, The University of Texas at Austin, Austin, TX, USA, [8]Byrd Polar Research Center and School of Earth Sciences, The Ohio State University, Columbus, OH, USA, [9]Jet Propulsion Laboratory, California Institute of Technology, Pasadena, CA, USA, [10]School of Earth and Environment, The University of Leeds, Leeds, UK

Abstract The upper mantle and transition zone beneath Antarctica and the surrounding oceans are among the poorest-imaged regions of the Earth's interior. Over the last 15 years, several large broadband regional seismic arrays have been deployed, as have new permanent seismic stations. Using data from 297 Antarctic and 26 additional seismic stations south of ~40°S, we image the seismic structure of the upper mantle and transition zone using adjoint tomography. Over the course of 20 iterations, we utilize phase observations from three-component seismograms containing *P*, *S*, Rayleigh, and Love waves, including reflections and overtones, generated by 270 earthquakes that occurred from 2001–2003 and 2007–2016. The new continental-scale seismic model (ANT-20) possesses regional-scale resolution south of 60°S. In East Antarctica, thinner continental lithosphere is found beneath areas of Dronning Maud Land and Enderby-Kemp Land. A continuous slow wave speed anomaly extends from the Balleny Islands through the western Ross Embayment and delineates areas of Cenozoic extension and volcanism that span both oceanic and continental regions. Slow wave speed anomalies are also imaged beneath Marie Byrd Land and along the Amundsen Sea Coast, extending to the Antarctic Peninsula. These anomalies are confined to the upper 200–250 km of the mantle, except in the vicinity of Marie Byrd Land where they extend into the transition zone and possibly deeper. Finally, slow wave speeds along the Amundsen Sea Coast link to deeper anomalies offshore, suggesting a possible connection with deeper mantle processes.

1. Introduction

Antarctica is the largest landmass covered by ice sheets, and thus provides a unique scale at which to study the interactions between large ice sheets and the solid Earth. Earth structure beneath the ice sheet influences ice dynamics in several important ways and plays a significant role in ice sheet evolution. Geothermal heat flow, a function of upper mantle temperature, lithospheric thickness, and crustal heat production, impacts whether the bed of the ice sheet is frozen or supports an active hydrologic system that can reduce basal friction, thereby increasing ice velocities (e.g., Pollard et al., 2005). Lithospheric thickness and upper mantle viscosity control the spatial and temporal scales of Glacial Isostatic Adjustment (GIA), determining whether the solid Earth response to ice mass change occurs across length scales of tens to many hundreds of kilometers, and over decades, hundreds, or thousands of years (e.g., Barletta et al., 2018; Kaufmann et al., 2005; Nield et al., 2014). GIA estimates are also important for determining the rate of ice mass loss in Antarctica because its rate of gravitational change greatly impacts satellite gravimetry of the Gravity Recovery and Climate Experiment (GRACE) (e.g., Groh et al., 2012; van der Wal et al., 2015). Recent modeling shows that the GIA response time is critical to both reconstructing past and present-day ice mass loss, and it may play a pivotal role in the evolution and stability of ice sheets into the future. In particular, the stability of marine-based ice sheets critically depends on the sub-ice topography (Gomez et al., 2015, 2018), and thus, solid Earth

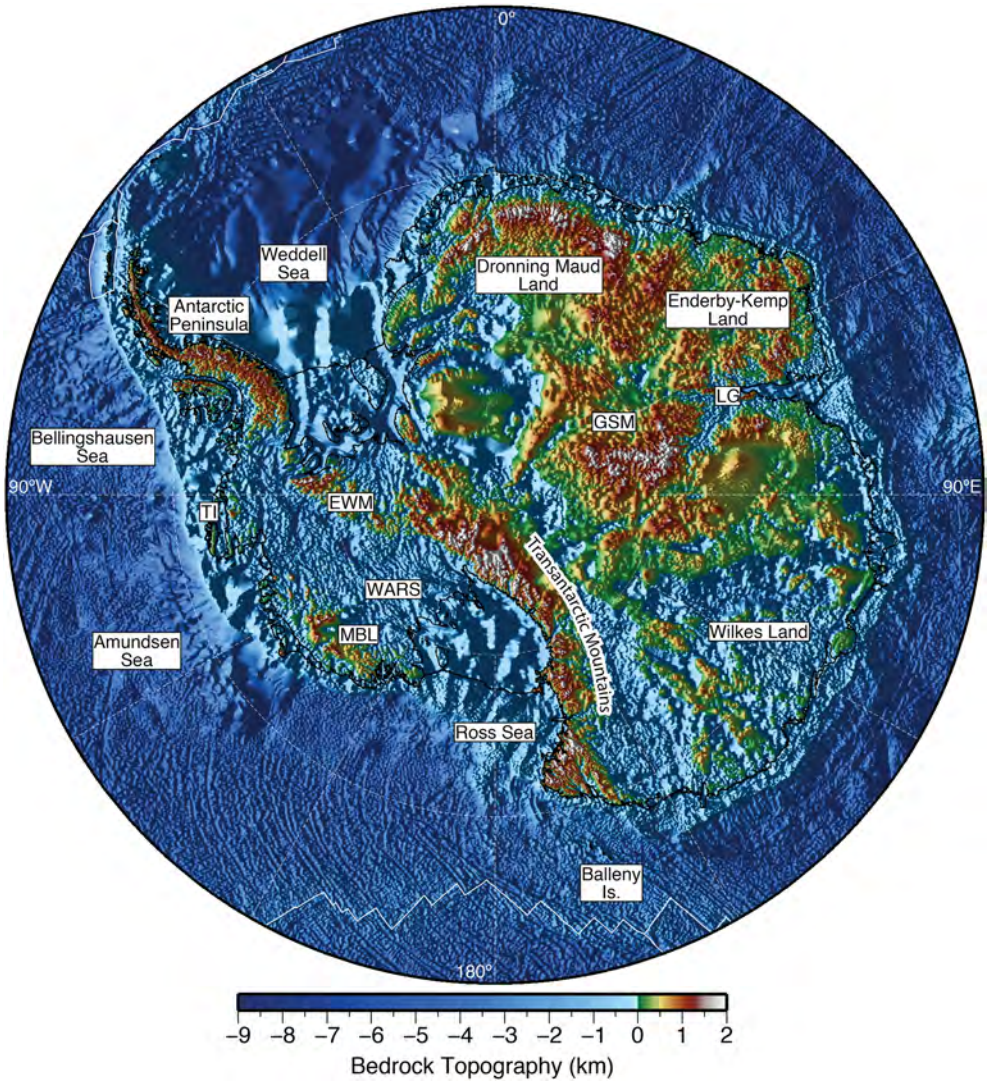

Figure 1. Map of Antarctica's subglacial bedrock topography and bathymetry (Fretwell et al., 2013). Abbreviations: EWM—Ellsworth Whitmore Mountains, GSM—Gamburtsev Subglacial Mountains, LG—Lambert graben, MBL—Marie Byrd Land, TI—Thurston Island, WARS—West Antarctic rift system.

structure and properties may have a profound impact on the stability of the West Antarctic Ice Sheet, and by extension, on the rate of sea level rise over the coming centuries (Adhikari et al., 2014; Barletta et al., 2018; Konrad et al., 2015).

The uniqueness of Antarctica and its ice sheets also leads to an incomplete documentation of the continent's geologic history and geophysical structure, thereby hindering our understanding of solid Earth-ice sheet interactions, sub-ice hydrology, seismicity, volcanism, and other key regimes. With rock exposures accounting for only ~0.18% of the total Antarctic landmass (Burton-Johnson et al., 2016), in situ geological sampling is severely limited and largely restricted to coastal regions, as well as the Ellsworth and Transantarctic Mountains (Figure 1). Thus, even fundamental geologic knowledge, such as the age of various sub-ice geographic provinces, is generally absent. For example, it is unclear whether most of East Antarctica is of Archean or early/late Proterozoic age and how its evolution is related to that of the other Gondwanan continents (e.g., Dalziel, 1992; Fitzsimons, 2003; Goodge et al., 2001; Goodge & Finn, 2010; Tingey, 1991). Similarly, the geological and geophysical causation, timing, and geographic extent of Mesozoic and Cenozoic rifting episodes in West Antarctica are incompletely known (e.g., Granot et al., 2013; Harry et al., 2018; Luyendyk, 1995; Siddoway, 2008). The physical inaccessibility of the sub-ice Antarctic solid

Earth compels indirect geological (e.g., detrital zircon chronology; Kelly & Harley, 2005) and, especially, geophysical methods, such as seismology, potential fields, and radar topography to reveal underlying structures and processes.

Seismology has proven to be a powerful tool for imaging solid Earth structure because of its versatility and high fidelity. Images of Earth's seismic structure not only aid in understanding geologic processes and geophysical structures but also constrain important parameters affecting solid Earth-ice sheet interactions. For instance, seismic wave speeds provide the best estimate of the mantle's thermal structure, which to first order controls heat flow at the bed of the ice sheet (Shapiro & Ritzwoller, 2004), and thus the rate and availability of water at the bed (Pattyn et al., 2016; Seroussi et al., 2017), as well as mantle viscosity and lithospheric thickness that control GIA (Ivins & Sammis, 1995; O'Donnell et al., 2017; Wu et al., 2012). To that end, recent studies are developing thermal models from seismological data to reveal first-order variations in heat flow, lithospheric thickness (An et al., 2015b), and mantle viscosity (Hay et al., 2017; van der Wal et al., 2015) across Antarctica.

Unfortunately, the Antarctic upper mantle and transition zone are among the most poorly imaged regions in the Earth's interior due to the scarcity of southern midlatitude landmasses and the challenges of operating seismic stations in extreme environments. This has severely limited the temporal and spatial extent over which high-quality broadband seismic data may be collected. Thus, advancement beyond the pioneering tomographic studies that first imaged the shear wave speed structure of the Antarctic upper mantle (Danesi & Morelli, 2001; Ritzwoller et al., 2001) and transition zone (Sieminski et al., 2003) has required a surge of seismic deployments targeting major tectonic features, such as the West Antarctic Rift System, the Transantarctic Mountains, and the Gamburtsev Subglacial Mountains (Figures 1 and 2). Ensuing seismological studies imaging the crust and upper mantle (e.g., Brenn et al., 2017; Chaput et al., 2014; Graw et al., 2016; Heeszel et al., 2016; Lawrence et al., 2006b; Lloyd et al., 2013, 2015; O'Donnell et al., 2019; Watson et al., 2006; White-Gaynor et al., 2019) and the transition zone (Emry et al., 2015; Reusch et al., 2008) at regional-scale resolution are of limited extent, leaving much of Antarctica insufficiently explored. By integrating high-quality broadband data from many such projects and from (sparse) permanent Antarctic stations, we can image the entire Antarctic mantle from the crust to the transition zone with the aid of adjoint tomography (e.g., Bozdağ et al., 2016; Chen et al., 2015; Fichtner et al., 2009; Tape et al., 2009, 2010; Zhu et al., 2015), which in this instance takes on the form of wave-equation traveltime tomography (Luo & Schuster, 1991).

This approach relies on high-performance computing combined with both numerical and adjoint methods to accurately determine synthetic three-component seismograms and sensitivity kernels. Simplifying assumptions, such as high-frequency asymptotic ray theory, are avoided by solving the weak formulation of the wave equation and simulating all complexities (e.g., anisotropy and attenuation) of seismic wave propagation within a complex 3-D medium (Faccioli et al., 1996, 1997; Komatitsch & Tromp, 2002a, 2002b; Komatitsch & Vilotte, 1998). When combined with adjoint methods, sensitivity kernels associated with different seismic model parameters can be efficiently computed with just two numerical wavefield simulations (e.g., Bamberger et al., 1982; Tape et al., 2007; Tarantola, 1984; Tromp et al., 2005). These waveforms need not be identified and may include three-component seismic waveforms containing *P*, *S*, Rayleigh, and Love waves, including reflections and overtones, which provide access to an abundance of waveform-encoded structural information that would traditionally be partitioned across several independent imaging techniques. The simultaneous use of these waveforms along with the accurate determination of synthetic seismograms and sensitivity kernels allows large swaths of Earth's elastic structure to be imaged at higher fidelity and resolution.

Using these tools, we produce the first tomographic model from the crust to the transition zone beneath Antarctica and the surrounding oceans, with sufficient resolution to connect tomographic features to dynamical advection of thermal or chemical heterogeneities. These first-of-a-kind images permit new constraints to be placed on not only geological and geophysical reconstructions encompassing the past ~100 million years but also the ancient East Antarctic lithosphere. This same model, ANT-20, is also uniquely suited for estimating solid Earth properties, such as geothermal heat flow, lithospheric thickness, and mantle viscosity. In this manuscript we emphasize the geologic interpretation of the tomographic images south of 60°S latitude. This includes the structure and evolution of the East Antarctic lithosphere and the West Antarctic

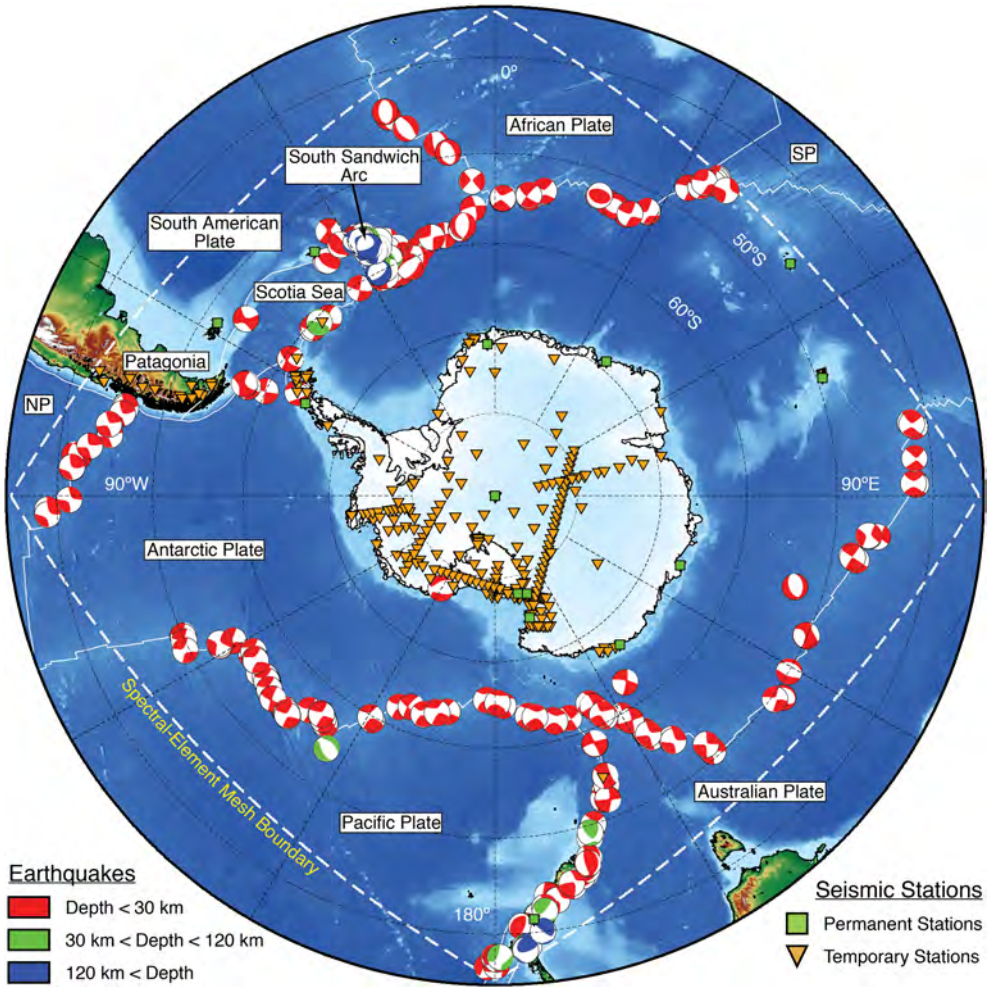

Figure 2. Map of the 323 broadband seismic stations and 270 earthquakes that are used in the adjoint tomographic inversion, which is performed in the area enclosed by the white dashed line. The focal mechanisms for earthquakes that occurred between 2007 and 2016 are from the global CMT catalog (global.cmt.org), while those for earthquake that occurred between 2001 and 2003 are from the spectral element moment tensor inversion discussed in section 3.3. In the background, we show the surface topography and bathymetry from ETOPO1 (Amante & Eakins, 2009). Thin white lines denote the plate boundaries (Bird, 2003), while the dashed black lines denote lines of latitude every 10° and lines of longitude every 30°. Abbreviations: NP—Nazca plate, SP—Somalia plate.

Rift System, Cenozoic volcanism in West Antarctica, and the Cenozoic subduction history of the Antarctic Peninsula.

2. Tectonic Setting and Previous Geophysical Studies

A distinction was illustrated by the continent's unique bimodal distribution of deglaciated surface topography (Cogley, 1984; O'Donnell & Nyblade, 2014), seismological structure (e.g., Danesi & Morelli, 2001; Ritzwoller et al., 2001), and geologic history (e.g., Boger, 2011; Dalziel & Elliot, 1982). These observations require the final assembly of East Antarctica by the early Paleozoic (e.g., Boger, 2011), indicate thick seismically fast lithosphere characteristic of a Precambrian Shield (e.g., Danesi & Morelli, 2001; Ritzwoller et al., 2001), and reveal anomalously high deglaciated modal elevation (~650 m; O'Donnell & Nyblade, 2014) relative to the other continents (Cogley, 1984). In contrast, it was not until the Cenozoic that West Antarctica began to reach its present-day configuration following multiple phases of extension (e.g., Dalziel & Elliot, 1982; Siddoway, 2008) and widespread volcanism (LeMasurier, 1990). These processes are associated with seismically slow and warm upper mantle (e.g., Danesi & Morelli, 2001; Ritzwoller et al., 2001) and are

paradoxically at odds with the anomalously low deglaciated modal elevation (approximately –450 m; Cogley, 1984; O'Donnell & Nyblade, 2014) of the region. Here we briefly review the geologic and geophysical studies that are making significant strides in refining these first-order observations of Antarctic tectonics.

2.1. East Antarctica

The geologic nature of East Antarctica, while poorly known, is essential for understanding the amalgamation and breakup of Gondwana, as it formed the core of the supercontinent. Although an ice sheet now covers much of the East Antarctic subcontinent, direct geologic sampling is still possible along the coast (e.g., Tingey, 1991) and within the Transantarctic Mountains (e.g., Goodge et al., 2001). These studies indicate that Archean to late Proterozoic outcrops dominate the peripheries of East Antarctica and that coastal outcrops correlate well with the conjugate terranes of the formerly juxtaposed African, Indian, and Australian continents (e.g., Boger, 2011; Fitzsimons, 2000a,b). Early tectonic reconstructions have therefore suggested that East Antarctica consists largely of an Archean nucleus that formed prior to or during the formation of Rodinia (Dalziel, 1991; Hoffman, 1991; Moores, 1991; Rogers et al., 1995; Tingey, 1991). The recognition of Neoproterozoic/early Paleozoic orogenic events along the coast and their possible inland continuation has led others (Boger, 2011; Fitzsimons, 2000a,b; Powell & Pisarevsky, 2002; Torsvik et al., 2008; Zhao et al., 1995) to instead propose the final assembly of East Antarctica during the early Paleozoic. This is further supported by the wealth of Archean to Cambrian detrital zircons that are believed to have originated from igneous and metamorphic rocks comprising the obscured terranes of East Antarctica (Veevers & Saeed, 2011, and references therein). Similarly, rock clasts and erratics found within glacial tills in the Transantarctic Mountains suggest the existence of Proterozoic terranes in central East Antarctica (Goodge et al., 2017). Although evidence suggests limited Phanerozoic tectonic activity in the East Antarctic interior, the peripheries have been affected by tectonic events such as the formation of the Lambert Graben (e.g., Phillips & Läufer, 2009) and the Transantarctic Mountains (e.g., Shen, Wiens, Stern et al., 2018; Stern & ten Brink, 1989), as well as the breakup of Gondwana (e.g., Boger, 2011).

This incomplete picture of East Antarctic tectonics provided by geologic studies is also captured by near-surface geophysical studies that, in part, seek to map the sub-ice continuations of major tectonic domains (e.g., Aitken et al., 2014; Ferraccioli et al., 2011; Ruppel et al., 2018). The deeper continental roots of these regions have in the past primarily been imaged by global- and continental-scale seismic tomography that reveal thick and fast lithosphere (e.g., Danesi & Morelli, 2001; Ritzwoller et al., 2001) but do not possess sufficient resolution to delineate tectonic provinces. Aided by additional seismological data, recent studies are now beginning to hint at lithospheric heterogeneity beneath East Antarctica (e.g., An et al., 2015a; Heeszel et al., 2013; Lloyd et al., 2013; Shen, Wiens, Anandakrishnan et al., 2018). For example, the mantle lithosphere beneath the Gamburtsev Subglacial Mountains (Figure 1) is seismically faster than to the north beneath the Lamber Graben (Heeszel et al., 2013) and to the south beneath the Polar Subglacial Basins (Heeszel et al., 2013; Lloyd et al., 2013). Regional studies also image variability in the extent of thick East Antarctic lithosphere relative to the Transantarctic Mountain front (e.g., Brenn et al., 2017; Graw et al., 2016; Lawrence et al., 2006a, 2006b; Watson et al., 2006).

2.2. West Antarctica

Our understanding of the geologic nature of West Antarctica is greater than that of the East Antarctic, yet it is still deficient in comparison to the other continents. Nonetheless, geologic and geophysical studies of the region reveal a complex history of long-lived subduction throughout the Phanerozoic (e.g., Cawood, 2005; Eagles, 2004) and multiple stages of continental extension since the mid-Jurassic (e.g., Dalziel et al., 2013; Siddoway, 2008; Wilson & Luyendyk, 2009). These events have led to the amalgamation and tectonic reorganization of at least four distinct West Antarctic crustal blocks, which are now separated by extended continental lithosphere of the Weddell Sea and the West Antarctic Rift System (Dalziel et al., 1982). Three of these crustal blocks, Marie Byrd Land, the Thurston Island-Eights Coast, and the Antarctic Peninsula (Figure 1), are forearc, and magmatic arc terranes that along with Zealandia and the Campbell Plateau formed the convergent central Pacific margin of Gondwana (Grunow et al., 1991; Mukasa & Dalziel, 2000). In contrast, the Ellsworth-Whitmore Mountains crustal block (Figure 1) may be a fragment of East Antarctica that underwent counterclockwise rotation and translation to its present-day relative position during the opening of the Weddell Sea (Grunow et al., 1987; Randall & Mac Niocaill, 2004; Schopf, 1969).

Whilst subduction along the central Pacific margin of Gondwana can be traced back to the Cambrian (Allibone & Wysoczanski, 2002) and continental extension initiated during the mid-Jurassic with the opening of the Weddell Sea (Dalziel et al., 2013), here we focus our attention on the tectonic evolution of West Antarctica since the late Cretaceous. Beginning at this time (~105–85 Ma), oblique subduction of the Phoenix plate waned as the stress regime transitioned from transpressional to transtensional, leading to widespread continental extension and rapid growth of the West Antarctic Rift System (Luyendyk, 1995; Luyendyk et al., 1996). This followed further extension and eventual sea floor spreading as Zealandia and the Campbell Plateau detached from West Antarctica (~83–70 Ma; Siddoway, 2008). Although subduction ceased as part of these events outboard of the Ross Sea sector of the West Antarctic Rift System and Marie Byrd Land, it continued along the Thurston Island-Eights Coast and the Antarctic Peninsula (Mukasa & Dalziel, 2000).

The first half of the Cenozoic brought about the main phase of uplift of the present-day Transantarctic Mountains (~55 Ma; Fitzgerald, 2002) and a further ~150–200 km of extension within the Ross Sea along the Transantarctic Mountain front (Cande & Stock, 2004; Wilson & Luyendyk, 2009). Sporadic extension continued within this region throughout the latter half of the Cenozoic (Granot et al., 2010) until possibly ceasing at ~11 Ma (Granot & Dyment, 2018). In contrast, during this time, the central West Antarctic underwent dextral strike-slip motion (Müller et al., 2007) or oblique convergence (Granot et al., 2013). A final stage of mid-Miocene to recent extension may have occurred in the Ross Sea within the Terror Rift (Fielding et al., 2008; Henrys et al., 2008), requiring a significant kinematic change to the rift system (Granot et al., 2010). This change may also be linked to inferred focused extension of narrow subglacial basins within central West Antarctica (Bingham et al., 2012; Jordan et al., 2010; LeMasurier, 2008; Lloyd et al., 2015; Winberry & Anandakrishnan, 2004). Currently, the West Antarctic Rift System appears to be dormant, as local seismic stations record sparse tectonic seismicity (Winberry & Anandakrishnan, 2003) and bedrock-based GPS indicate no resolvable extension (Donnellan & Luyendyk, 2004; Wilson et al., 2015).

During the Cenozoic, West Antarctica also experienced widespread volcanism that is observed from the Antarctic Peninsula, across central West Antarctica, and along the Transantarctic Mountains (e.g., LeMasurier, 1990). Specifically, volcanism in the Antarctic Peninsula is diagnostic of a slab window (Smellie, 1987), which formed as subduction of the Phoenix plate ceased from west to east along the Thurston Island-Eights Coast and the Antarctic Peninsula throughout the Cenozoic (Eagles et al., 2004, 2009; Larter et al., 1997). In central West Antarctica, domal uplift of Marie Byrd Land occurred at ~29–25 Ma (LeMasurier & Landis, 1996), leading to the development of a volcanic province consisting of three linear volcanic chains and numerous other volcanic edifices (LeMasurier & Rex, 1989; Panter et al., 1994). Furthermore, volcanism is observed in the Amundsen Sea Embayment (LeMasurier, 1990) and is geophysically inferred in the sub-ice regions of the West Antarctic Rift System (e.g., Behrendt et al., 1996). Finally, along the Transantarctic Mountains, volcanism extends from Mt. Mourning, ~100 km south of Ross Island, northward along the length of the mountain range (Kyle, 1990; LeMasurier, 1990; Phillips et al., 2018), except for two outliers in the southern Transantarctic Mountains (Stump et al., 1980).

Early Tomographic models (e.g., Danesi & Morelli, 2001; Ritzwoller et al., 2001) lack the resolution necessary to image the upper mantle structures alluded to by geologic and near-surface geophysical studies. Instead, images reveal slow wave speeds across West Antarctica that extend to 200 km depth, except beneath the Marie Byrd Land coast, the Ross Sea, and the Balleny Islands where these features continue into the transition zone (Sieminski et al., 2003). Recent continental tomographic inversions (An et al., 2015a; Hansen et al., 2014) achieve higher resolution, but the greatest insights are gained by still higher resolution regional models. Although these models only reveal patches of the West Antarctic, they indicate variable upper mantle wave speeds that coincide with the West Antarctic crustal blocks (Heeszel et al., 2016; Lloyd et al., 2015), distinguish between zones of late Cretaceous/early Cenozoic and late Cenozoic extension within the West Antarctic Rift System (e.g., Heeszel et al., 2016; Lloyd et al., 2015; Shen, Wiens, Anandakrishnan et al., 2018; White Gaynor et al., 2019), and reveal warmer upper mantle beneath late Cenozoic volcanism (e.g., Heeszel et al., 2016; Lloyd et al., 2015; Watson et al., 2006). The most prominent features include slow wave speeds along the Transantarctic Mountain front and those beneath the Marie Byrd Land volcanic dome. However, the lateral and radial extent of these features remains unclear, while some regions of West Antarctica have yet to be imaged at similar resolution.

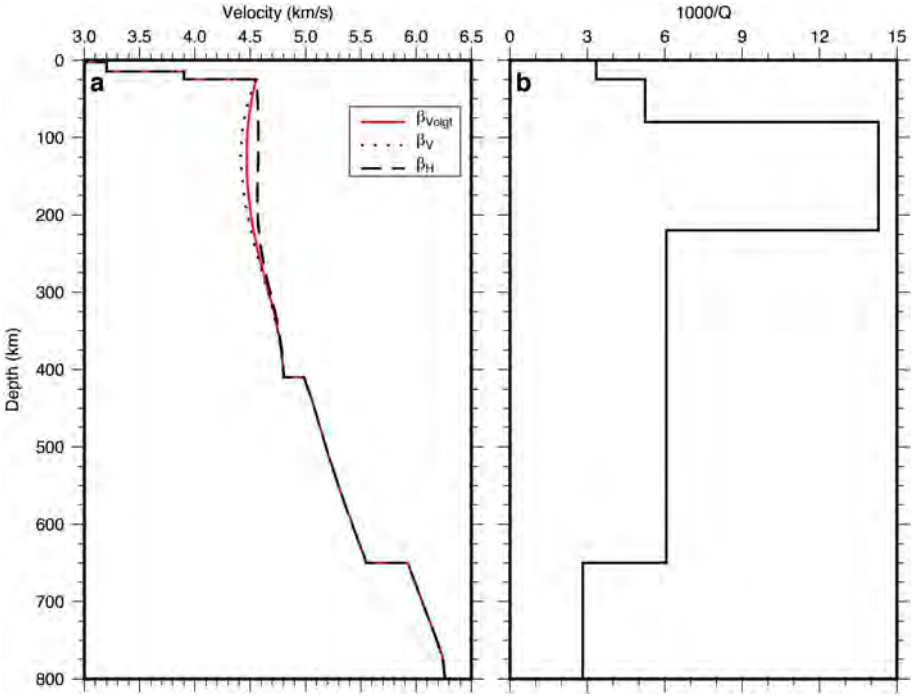

Figure 3. (a) Horizontally (dashed line) and vertically (dotted line) polarized shear wave speeds from the 1-D reference Earth model STW105 (Kustowski et al., 2008), which are used to compute the Voigt average shear-wave speed reference (red line). (b) the 1-D attenuation model QL6 (Durek & Ekström, 1996) used in the wavefield simulations.

3. Data and Methodology

3.1. Station and Earthquake Database

We utilize 270 earthquakes and 323 broadband seismic stations (Table S1 in the supporting information) to image the upper mantle and transition zone beneath Antarctica and portions of the southern midlatitude oceans (Figure 2). In doing so, we take advantage of the dramatic improvement in Antarctic seismic instrumentation since the turn of the 21st century, which by the end of 2016 has brought about the deployment and operation of over 300 broadband seismic stations. For this study, we obtained data from 297 of these stations, many of which operated continuously for two or more years as part of temporary regional arrays, such as TAMSEIS (2001–2003; Lawrence, et al., 2006b), GAMSEIS (2007–2009; Lloyd et al., 2013), POLENET/A-NET (2007 to present; Lloyd et al., 2015), TAMNNET (2012–2015; Hansen et al., 2015), and RIS (2013–2016; Chaput et al., 2018). Besides these deployments, numerous other seismic stations have also operated on the continent, providing invaluable coverage in regions not sampled by the temporary regional arrays.

In addition, we supplement the Antarctic seismic data sets with waveforms from 26 broadband seismic stations south of ~40°S latitude (Figure 2). The majority of these stations are located in Patagonia or on islands fringing the Scotia Sea, while only four are located elsewhere on islands in the southern oceans. The poor station distribution between ~40° and 65°S reflects landmass scarcity, and thus, it is fortunate that the earthquake distribution in this study heavily samples this region of the southern oceans (Figure 2).

Focusing on the time periods when temporary regional seismic arrays were operating in Antarctica (2001–2003 and 2007–2016), we select 270 earthquakes with moment magnitudes of 5.5 to 7.0 (Figure 2). These time periods are further subdivided into five groups that capture the evolving broadband seismic station distribution across the Antarctic. Within each group, larger earthquakes possessing good signal to noise are qualitatively chosen, while simultaneously achieving the most widespread geographic earthquake distribution in the study region. The majority of the earthquakes are shallow, occurring at depths less than 30 km and along the mid-ocean ridges that form much of the Antarctic plate boundary. Only a single earthquake is located within the Antarctic continent, and deeper earthquakes are mostly restricted to the South Sandwich Arc and along the Australian/Pacific plate boundary (Figure 2).

3.2. The Starting Model and Spectral Element Mesh

We utilize a 3-D starting model that is mapped to a spectral element representation of the globe (Komatitsch & Tromp, 2002a, 2002b), on which seismic wave propagation is simulated to refine the centroid moment tensors (section 3.3). This same 3-D starting model is also mapped to a regional spectral element mesh (Chen et al., 2015; Zhu et al., 2015) and is used in numerical wavefield simulations during the adjoint tomographic inversion (section 3.4). Our 3-D starting Earth model, hereafter ANT-00, is constructed from a modified version of CRUST1.0 (Laske et al., 2013), which approximates the Antarctic ice and crustal structure, and from the global mantle model S362ANI (Kustowski et al., 2008). S362ANI provides long-wavelength structure for radially anisotropic compressional-wave and shear-wave speeds (α_v, α_h, β_v, and β_h) within the mantle, as well as topography of the transition zone discontinuities. Kustowski et al. (2008) determined these parameters with respect to their own 1-D reference Earth model, STW105 (Figure 3a), from which we also obtain density (ρ) and the dimensionless anisotropic parameter η. Finally, like Kustowski et al. (2008), we adopt the 1-D attenuation model QL6 (Figure 3b; Durek & Ekström, 1996). This same mantle structure has been used successfully as part of the 3-D starting Earth model in both regional and global adjoint tomographic inversions (Bozdağ et al., 2016; Chen et al., 2015; Zhu et al., 2015) and is routinely used to compute spectral element synthetic seismograms for global earthquakes in near real time (Tromp et al., 2010).

Within the crust, we parameterize ANT-00 in terms of isotropic compressional-wave and shear-wave speed (α and β), as well as ρ. These parameters are updated simultaneously, along with those of the mantle, similar to previous adjoint tomographic studies (Bozdağ et al., 2016; Chen et al., 2015; Zhu et al., 2015). We obtain the initial values of these parameters from the ice layer, the three sedimentary layers, and the three crystalline crustal layers of CRUST1.0 (Laske et al., 2013). However, recent geophysical studies of the Antarctic crustal structure (e.g., An et al., 2015a; Chaput et al., 2014; O'Donnell & Nyblade, 2014; Shen, Wiens, Anandakrishnan et al., 2018) indicate that CRUST1.0 inadequately constrains the Moho topography across the Antarctic continent. This is reflected, in part, by its failure to capture the thinned crust of the West Antarctic Rift System and the thick crustal roots that underlie portions of East Antarctica. Therefore, a more realistic model of Moho topography is incorporated into ANT-00 by adjusting the thickness of the lower crustal layer(s) of CRUST1.0 to match the Moho topography inferred by the surface wave study of An et al. (2015a), which was partially constrained by Moho depth estimates from receiver functions (.g., Reading, 2006; Hansen et al., 2009, 2010; Chaput et al., 2014) and from active source seismic studies (e.g., Bayer et al., 2009; Trey et al., 1999). Likewise, the surface and bedrock topography of Antarctica is updated using BEDMAP2 (Fretwell et al., 2013).

We map ANT-00 to both a global and regional spectral element mesh using a cubed-sphere mapping (Komatitsch & Tromp, 2002a; Ronchi et al., 1996), which maintains a similar number of spectral elements per wavelength throughout the mesh. The spectral elements are deformed to account for topography, bathymetry, and ellipticity and, where possible, honor first- and second-order seismic discontinuities (Komatitsch & Tromp, 2002a, 2002b; Tromp et al., 2010). Efficient use of high-performance computing is achieved by discretizing the global and regional meshes to just resolve the minimum period utilized in the spectral element moment tensor relocations and the adjoint tomographic inversion. The regional mesh consists of a single cubed-sphere chunk that is composed of 288-by-288 spectral elements at its free surface. The spectral elements contain five Gauss-Lobatto-Legendre interpolation points (Canuto et al., 1988, p. 61) in each orthogonal direction, allowing waveforms to be resolved down to a period of ~15 s. We center the regional mesh at 90°S and rotate it by 45° to achieve the best possible geographic distribution of earthquakes and stations (Figure 2).

Lastly, a key challenge in constructing the spectral element mesh is maintaining adequate sampling within the crust while still honoring the strongly varying Moho topography. We achieve this by using a single layer of spectral elements to honor thin, predominantly oceanic crust, and two to three layers of spectral elements to accommodate thicker continental crust, as was done in previous studies (e.g., Tromp et al., 2010; Zhu et al., 2015). In this study, the spectral element mesh realistically models the Moho at depths shallower than 15 km and between 22- and 50-km depth. Otherwise, the Moho is represented within the spectral elements using the Gauss-Lobatto-Legendre interpolation points. A unique challenge to the construction of the spectral element mesh arises from the Antarctic ice sheet, as it has a mean thickness of ~2.1 km and has thicknesses in excess of 3 km across much of East Antarctica (Fretwell et al., 2013). The Antarctic ice sheet

strongly influences surface wave velocities at both short and intermediate periods (Ritzwoller et al., 2001). Therefore, across much of Antarctica the first layer of spectral elements is held fixed at 10 km, allowing the Antarctic ice sheet to be coarsely captured by the Gauss-Lobatto-Legendre interpolation points, which have an average vertical spacing of 2.5 km.

3.3. Earthquake Source Parameters

We obtain the source parameters for each earthquake from the Global Centroid-Moment-Tensor (CMT) catalog (global.cmt.org; Ekström et al., 2012), which includes the earthquake's origin time, half duration, centroid location, and moment tensor solution. Previous adjoint tomographic studies (Bozdağ et al., 2016; Chen et al., 2015; Zhu et al., 2015) have refined a subset of these parameters (moment tensor solution, depth, latitude, and longitude) through a computationally intensive CMT inversion based on the spectral element method (Liu et al., 2004). Typically, these inversions reduce the scalar moment and shift the centroid by less than 10 km. This often includes 3–8 km of shallowing and helps to offset a CMT catalog bias toward deeper earthquake depths (Hjörleifsdóttir & Ekström, 2010). Despite the benefits, it is challenging to justify the high computational cost (~1 million CPU hours) required to refine the CMT solution for all 270 earthquakes when the typical centroid shift is less than one fifth of the crustal wavelength of the shortest period waveforms ($T = 15$ s) utilized in the inversion. To investigate this, we performed the inversion on a subset of our earthquakes and confirmed only small changes to the centroid and moment tensor parameters, thus justifying our decision to use the original CMT solutions in this study.

Earthquakes occurring prior to 2004, for which CMT solutions have not been determined with intermediate period surface waves (Ekström et al., 2012), may have less well-resolved parameters. They may thus benefit from the spectral element CMT inversion, as waveforms from both long-period body waves and intermediate-period surface waves are utilized. Therefore, we inverted all 32 earthquakes in our database that occur prior to 2004 using the spectral element CMT algorithm developed by Liu et al. (2004). This algorithm refines a subset of the source parameters (six unique moment tensor components, depth, latitude, and longitude) by minimizing the nondimensional least squares waveform differences between observed and synthetic three-component seismograms. To that end, the spectral element solver SPECFEM3D_GLOBE (Komatitsch & Tromp, 2002a, 2002b) is used to simulate seismic wave propagation down to a period of 30 s within the ANT-00 global mesh in order to compute 100-min synthetic seismograms for the initial CMT solution. For these inversions, we utilize measurement windows containing long-period body waves (30 s $\leq T \leq$ 80 s) and intermediate-period surface waves (80 s $\leq T \leq$ 120 s) that are recorded by a global distribution of broadband seismic stations (FDSN Network Codes G, GE, II, and IU) and are identified, in part, on the basis of observed and synthetic waveform similarity using the automated window selection tool FLEXWIN (Maggi et al., 2009).

As part of the source inversion algorithm (Liu et al., 2004), we require that the earthquake not produce any change in volume (i.e., the moment tensor has zero trace) and explore whether we can attain further improvement by prescribing a double-couple source (i.e., the determinant of the moment tensor is zero). We then invert for just the moment tensor, the moment tensor plus depth, and the moment tensor plus centroid. Of these six variants, the source parameters that maximize the variance reduction are taken as the new CMT solution. The 32 spectral element CMT inversions give rise to changes in source parameters similar to those reported in previous studies (Bozdağ et al., 2016; Chen et al., 2015; Zhu et al., 2015).

3.4. Adjoint Inversion for Seismic Structure

We utilize frequency-dependent phase differences between observed and synthetic three-component seismograms, along with adjoint tomographic techniques (e.g., Luo & Schuster, 1991; Tape et al., 2007; Tromp et al., 2005; Zhu et al., 2015), to image the seismic structure of both the crust and mantle beneath Antarctica and surrounding ocean basins (Figure 2). In doing so, we assume that the crust is isotropic (α and β), while the mantle is taken to be radially anisotropic (α_v, α_h, β_v, β_h, and η). Furthermore, by assuming that the bulk modulus (κ) is isotropic, and thus radial anisotropy arises exclusively from the shear modulus (μ), we may recast the compressional-wave speeds (α_v and α_h) in terms of isotropic bulk sound wave speed (c) and the shear-wave speeds (β_v and β_h). This reduces the model parameters considered in the adjoint

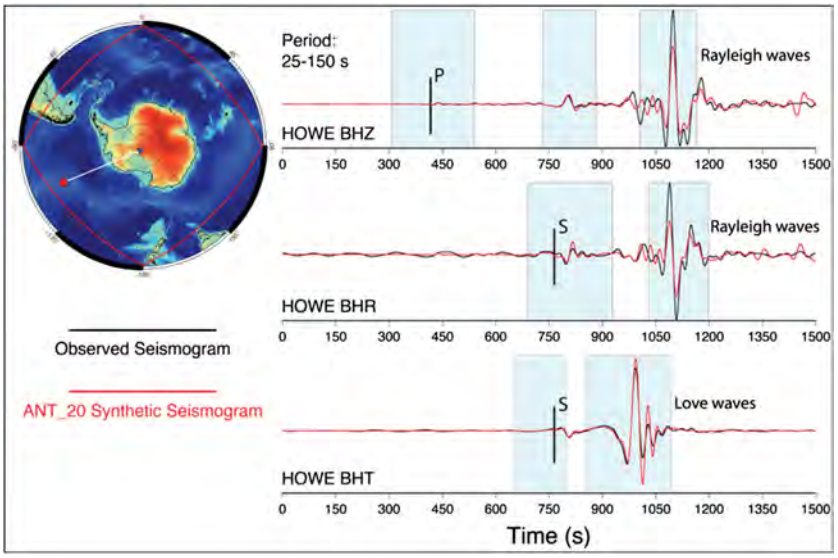

Figure 4. An example of synthetic (red) and observed (black) three-component seismograms used in the 20th iteration of the adjoint tomographic inversion. The blue boxes identify measurement windows utilized in the inversion. A map of surface topography and bathymetry (Amante and Eakins, 2009) on the left shows the path between the earthquake epicenter (red circle) and seismic station HOWE (blue triangle).

inversion to c, β_v, β_h, and η. Finally, although we do not invert for density (ρ), it is iteratively updated using the following empirical relationship from Montagner and Anderson (1989),

$$\delta \ln \rho = 0.33 \delta \ln \beta_{\text{Voigt}}, \tag{1}$$

and β_{Voigt} is the Voigt average of the radially anisotropic shear-wave speeds (Babuska & Cara, 1991):

$$\beta_{\text{Voigt}} = \sqrt{\frac{2\beta_v^2 + \beta_h^2}{3}}. \tag{2}$$

The adjoint tomographic inversion leverages the spectral element solver SPECFEM3D_GLOBE (Komatitsch & Tromp, 2002a, 2002b) and its ability to efficiently simulate all complexities of seismic wave propagation (Komatitsch & Tromp, 1999) in order to iteratively refine the Earth's structure. We begin by simulating the seismic wavefield produced by each of the 270 earthquakes within the regional mesh, by first using the starting model ANT-00 and thereafter the updated model from the prior iteration, to obtain 55-min synthetic three-component displacement seismograms for each of the 323 broadband seismic stations. In preparation for identifying the measurement windows, a Gaussian moment-rate function with a width of approximately twice the CMT solution's half duration is convolved with the synthetic seismograms, while the instrument responses are removed from the observed seismograms. Both the observed and synthetic seismograms are then filtered, resampled at 10 Hz, and their horizontals are rotated to obtain the radial and transverse components. We use FLEXWIN (Maggi et al., 2009) to identify measurement windows on all three components (Z, R, and T) and within two period bands: a short-period band (15 s $\leq T \leq$ 50 s) targets body waves and a long-period band (initially 50 s $\leq T \leq$ 150 s) targets both body and surface waves (Figure 4). As the fit between the observed and synthetic seismograms improves, and thus the elastic structure is further refined, the short-period corner of the long-period band is gradually reduced from 50 to 25 s (Figure 5a).

For each window, the traveltime difference and a nondimensional phase misfit between the observed and synthetic seismogram is measured preferentially with frequency-dependent multitaper techniques (Laske & Masters, 1998; Zhou et al., 2004) or else by cross correlation. The nondimensional multitaper phase misfit may be expressed as

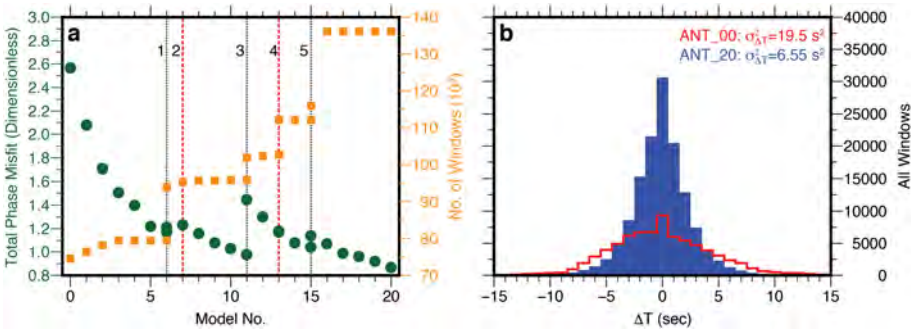

Figure 5. (a) Evolution of the total phase misfit (green circles) and the total number of measurement windows (orange squares) as a function of the model number. The black dotted lines indicate when the short-period corner of the long-period band was decreased from (1) 50 to 40 s, (3) then to 30 s, and (5) finally to 25 s. the red dashed lines indicate (2) when seismic data from international stations located in East Antarctica and (4) when new earthquake waveforms recorded in 2016 were added to the adjoint inversion. (b) Histograms of the traveltime phase differences between the observed and synthetic seismograms along with their variances ($\sigma^2_{\Delta T}$) are shown for the starting model ANT-00 (red) and the final model ANT-20 (blue). Figures S1 and S2 show similar plots for each of the six measurement categories.

$$\chi = \frac{1}{2}\int w(\omega)\left(\frac{\tau(\omega,\boldsymbol{m})}{\sigma(\omega)}\right)^2 d\omega, \tag{3}$$

where $w(\omega)$ represents a windowing filter, $\Delta\tau(\omega,\boldsymbol{m})$ is the frequency-dependent traveltime difference, and $\sigma(\omega)$ is the standard deviation of the observed and the reconstructed synthetic seismograms. For frequency-independent measurements, equation (3) reduces to the cross-correlation phase misfit function. The total phase misfit (Figure 5a) gives equal weight to the phase misfit from each of the six measurement categories (Figure S1) and by extension to each earthquake. Perhaps most importantly, the choice of the misfit function directly impacts the form of the adjoint source and thus the information conveyed by the sensitivity kernels (Tromp et al., 2005; Yuan et al., 2016).

The gradient of the total phase misfit function with respect to the model parameters may also be written as

$$\delta\chi_{\text{total}} = \int_V \left[K_c\delta\ln c + K_{\beta_v}\delta\ln\beta_v + K_{\beta_h}\delta\ln\beta_h + K_\eta\delta\ln\eta\right]dV, \tag{4}$$

where K_i are summed, preconditioned, and smoothed traveltime event sensitivity kernels with respect to the model parameters that fully account for the anelasticity arising from the attenuation model QL6 (Durek & Ekström, 1996). For each earthquake, these kernels are calculated by way of two numerical simulations: A forward wavefield simulation using the earthquake source and a time-reversed adjoint wavefield simulation consisting of fictitious three-component adjoint sources placed at the seismic stations (Komatitsch et al., 2016; Tromp et al., 2005). In order to better balance the sensitivity kernels, and thus data coverage, we follow Zhu et al. (2015) and divide by a preconditioner based on the forward ($\boldsymbol{s}$) and adjoint ($\boldsymbol{s}^\dagger$) wavefield accelerations,

$$H_{\text{Approx}}(\boldsymbol{x}) = \int \partial_t^2\boldsymbol{s}(\boldsymbol{x},t)\cdot\partial_t^2\boldsymbol{s}^\dagger(\boldsymbol{x},T-t)dt, \tag{5}$$

which also approximates the diagonals of the Hessian matrix—a square matrix of second-order partial derivatives of the misfit function with respect to density. Lastly, the kernels are convolved with a 3-D Gaussian smoothing operator in which the radial half width is 15 km (smoothing length: ~45 km) and the lateral half width varies with depth and model iteration. Within the upper mantle, the lateral half width decreases from 100 to 50 km (smoothing length: ~280 and ~140 km, respectively) in unison with the reduction of the short-period corner of the long-period band, while within the transition zone and lower mantle, the lateral half width is held fixed at 120 and 150 km, respectively (smoothing length: ~340 and ~425 km, respectively).

Finally, we update the model by determining the search direction and step length necessary to minimize the misfit function. For the first iteration, the search direction is aligned by the negative of the gradient (equation (4)), while in subsequent iterations, it is determined from the current gradient and the search

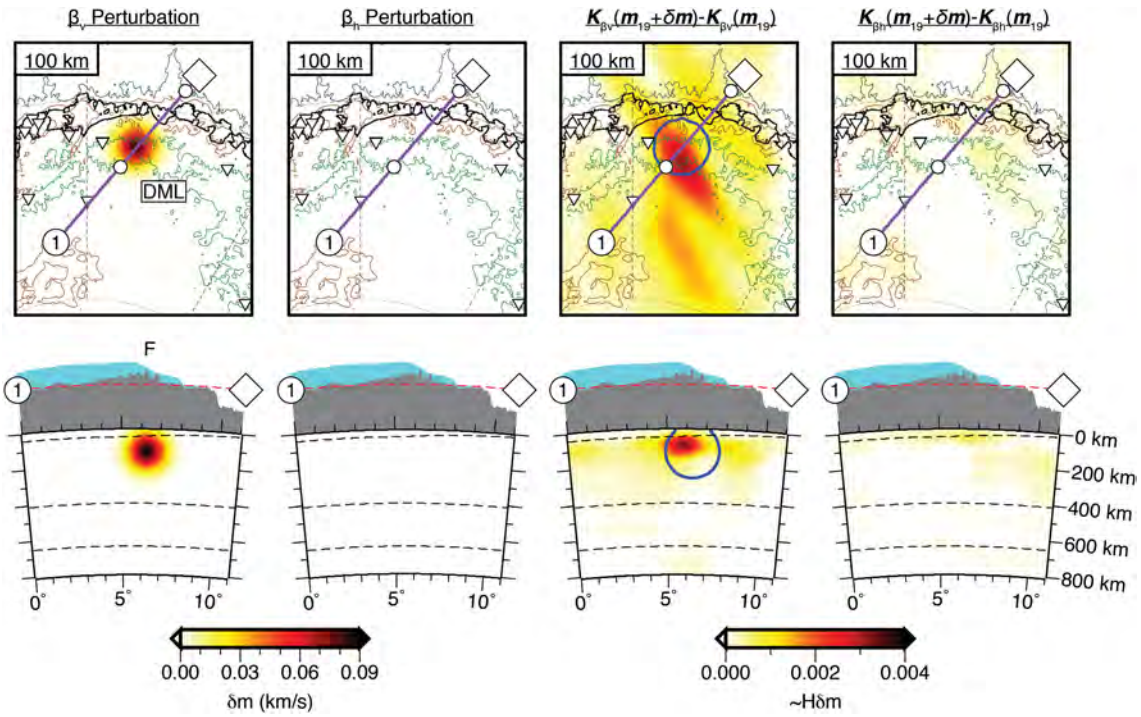

Figure 6. Horizontal and vertical slices from a point-spread function test that is centered on the Fimbulheimen Mountains of Dronning Maud land. The first two columns show the localized model perturbation to the β_v and β_h components. Note that we only perturb the β_v component using a spherical Gaussian anomaly with a half width of ~120 km and a peak amplitude of 0.09 km/s. The last two columns show the point-spread functions (K_{β_v} and K_{β_h}). In the third column the blue line shows the 0.01-km/s contour of the localized model perturbation. The horizontal slices are at 100-km depth and also depicts bathymetry and bedrock topography contours for 1,000 m (thin green line) and −500 m (thin brown line), as well as −2,500 m (thin dark gray line) in the oceans (Fretwell et al., 2013). Thicker red lines denote the plate boundaries (Bird, 2003), while thin dashed black lines are lines of latitude every 10° or lines of longitude every 30°. Within the main plot of the vertical slices the dashed black lines indicate the Moho topography (section 3.2) and a uniform 410- and 650-km seismic discontinuity. Atop of each vertical slice is the exaggerated bedrock (gray) and surface (cyan) topography with the red dashed line indicating sea level. Abbreviations: DML—Dronning Maud land, F—Fimbulheimen.

direction of the prior iteration using a conjugate gradient approach (Fletcher & Reeves, 1964). The optimal step length, and thus the model update, is determined by a line search that tests several candidate models to identify which minimizes the phase misfit for a subset of 18 geographically and temporally well-distributed earthquakes. Following 20 preconditioned conjugate gradient iterations, we arrive at the current model, ANT-20, which reduces both the total phase misfit and the variance of the observed and synthetic traveltime differences by a factor of 3 (Figure 5). The evolution of these parameters for each of the six measurement categories can also be viewed in Figures S1 and S2. By the final iterations of the inversion each successive iteration results in a relatively small reduction to the total phase misfit, suggesting further improvement of the model will require more complex parameterization that more fully and accurately accounts for anisotropy and anelasticity (Zhu et al., 2015).

4. Results

4.1. Resolution Analysis

Traditional tomographic studies often rely on synthetic model recovery tests (e.g., Lloyd et al., 2013, 2015) and in some instances utilize Monte Carlo techniques (e.g., Shen, Wiens, Anandakrishnan et al., 2018) to assess model recovery and reliability. Both approaches rely on the ability to quickly and efficiently solve the forward and inverse problem. These approaches are not practical in adjoint tomography as each additional inversion carries the same (considerable) computational cost as the initial tomographic inversion. However, it is still possible to obtain some insight into the reliability of the tomographic model ANT-20 by performing point-spread function tests (Fichtner & Trampert, 2011) or by stochastically probing the

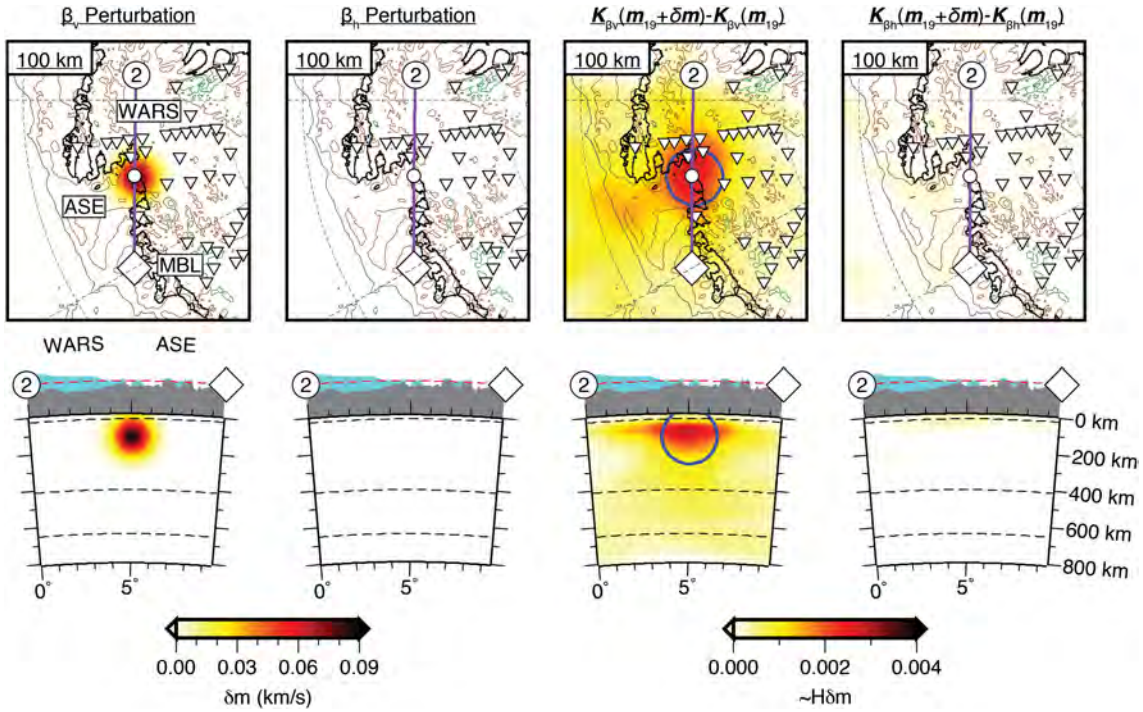

Figure 7. Horizontal and vertical slices from a point-spread function test that is centered on the Amundsen Sea embayment. The first two columns show the localized model perturbation in the β_v and β_h components. Note that we once again only perturb the β_v component using a spherical Gaussian anomaly with a half width of ~120 km and a peak amplitude of 0.09 km/s. The last two columns show the point-spread functions (K_{β_v} and K_{β_h}). The details of each plot are similar to Figure 6. ABBREVIATIONS: ASE—Amundsen Sea EMBAYMENT, MBL—Marie Byrd Land, WARS—West Antarctic rift system.

Hessian matrix (Fichtner & Leeuwen, 2015). Here we present three targeted point-spread function tests and also examine the approximate diagonal Hessian matrix—a proxy for relative data coverage.

Following Fichtner and Trampert (2011), point-spread function tests are utilized to assess the curvature of the misfit function and thus the degree of blurring, both spatially and across different types of model parameters, due to a localized model perturbation. Because the Hessian matrix is not easily calculated, its action on a localized model perturbation is determined using a finite difference approximation of the gradient:

$$\boldsymbol{H}\cdot\delta\boldsymbol{m}\approx\delta\chi_{\text{total}}(\boldsymbol{m}+\delta\boldsymbol{m})-\delta\chi_{\text{total}}(\boldsymbol{m}), \tag{6}$$

where $\boldsymbol{H}$ is the Hessian matrix, $\delta\boldsymbol{m}$ is the localized model perturbation, and $\delta\chi_{\text{total}}$ is the misfit gradient evaluated for both models $\boldsymbol{m}$ and $\boldsymbol{m}+\delta\boldsymbol{m}$. The gradient $\delta\chi_{\text{total}}(\boldsymbol{m})$ is available from the tomographic inversion and only the perturbed gradient $\delta\chi_{\text{total}}(\boldsymbol{m}+\delta\boldsymbol{m})$ needs to be determined. This requires the same computational cost as a single tomographic iteration, and therefore only a handful of these tests can be realistically performed.

We conduct two point-spread function tests in which a single localized β_v perturbation is added to the penultimate model, ANT-19, in the Fimbulheimen Mountains of Dronning Maud Land (Figures 6) and the Amundsen Sea Embayment (Figures 7). In both instances, a spherical Gaussian model perturbation with a maximum amplitude of 0.09 km/s and a half width of ~120 km is placed near 100-km depth. Each localized model perturbation is reasonably well preserved in the point-spread function, despite exhibiting some degree of blurring due to smoothing of the preconditioned gradients and the resolution limits imposed by the geographic distribution of earthquakes and stations. For example, in the Fimbulheimen Mountains (Figures 6) the point-spread function for β_v is characterized by predominantly lateral inland smearing in the direction of more limited seismic coverage (Figure 2). Equally important is the near absence of features in the point-spread functions for β_h (Figures 6), which indicates minimal cross contamination between β_v and β_h in ANT-20. These results are roughly similar to the point-spread function test conducted in the Amundsen Sea Embayment (Figure 7).

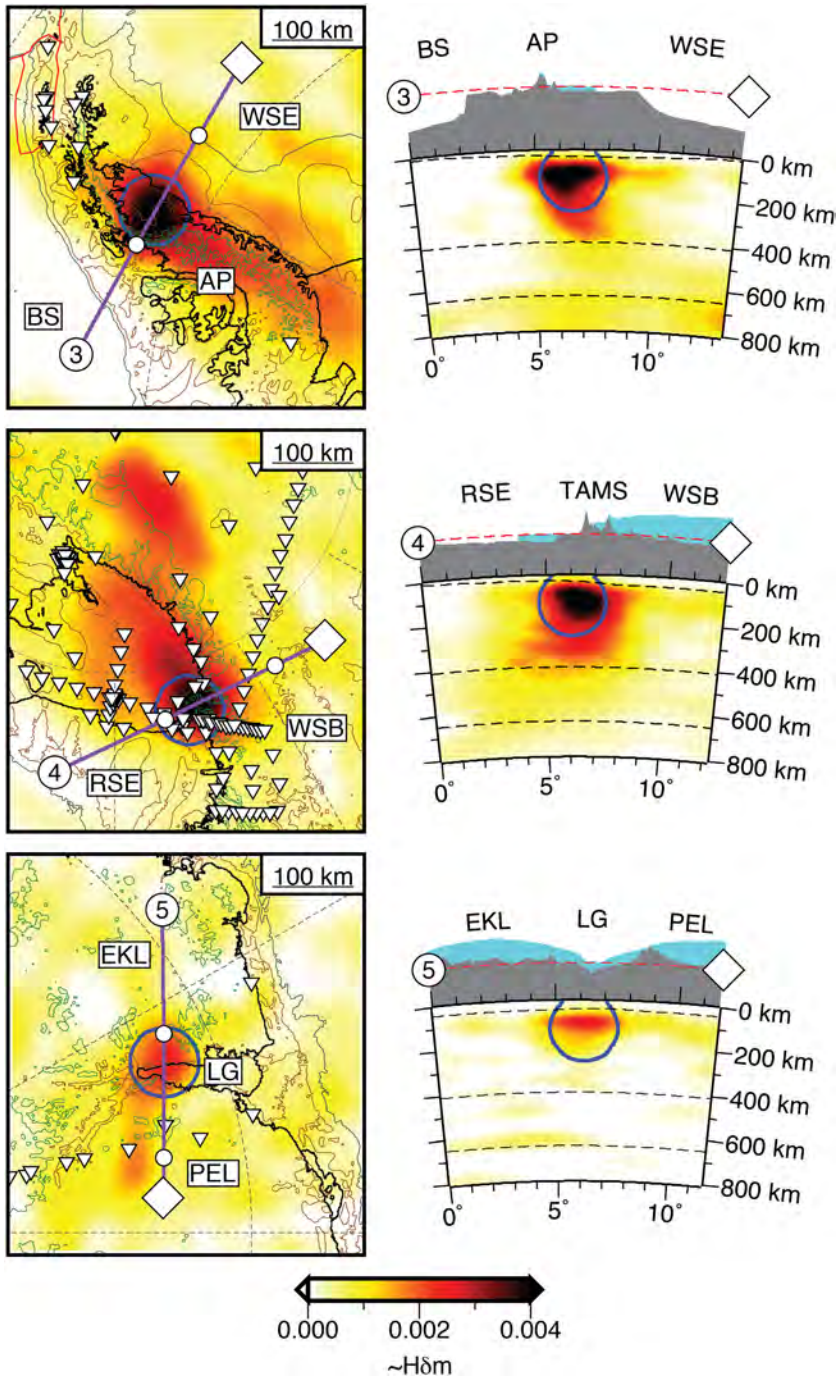

Figure 8. Horizontal and vertical slices from a point-spread function test consisting of three localized model perturbations that are located beneath the Antarctic Peninsula, Ross Island, and the Lambert Graben. The model perturbations are applied to only the β_v component, and each is identical to the perturbation used in Figures 6 and 7. Unlike Figures 6 and 7, we show only the point-spread function K_{β_v} and indicate the 0.01-km/s contour of the localized model perturbations. The details of each plot are similar to Figure 6. Abbreviations: AP—Antarctic Peninsula, BS—Bellingshausen Sea, EKL—Enderby-Kemp Land, LG—Lambert Graben, PEL—Princess Elizabeth Land, RSE—Ross Sea Embayment, TAMS—Transantarctic Mountains, WSB Wilkes Subglacial Basin, WSE—Weddell Sea Embayment.

To further probe the Hessian matrix across Antarctica, we perform a point-spread function test that introduces localized β_v perturbations beneath the Antarctic Peninsula, Ross Island, and the Lambert Graben. The extent, amplitude, and depth of these localized model perturbations are identical to those used in the

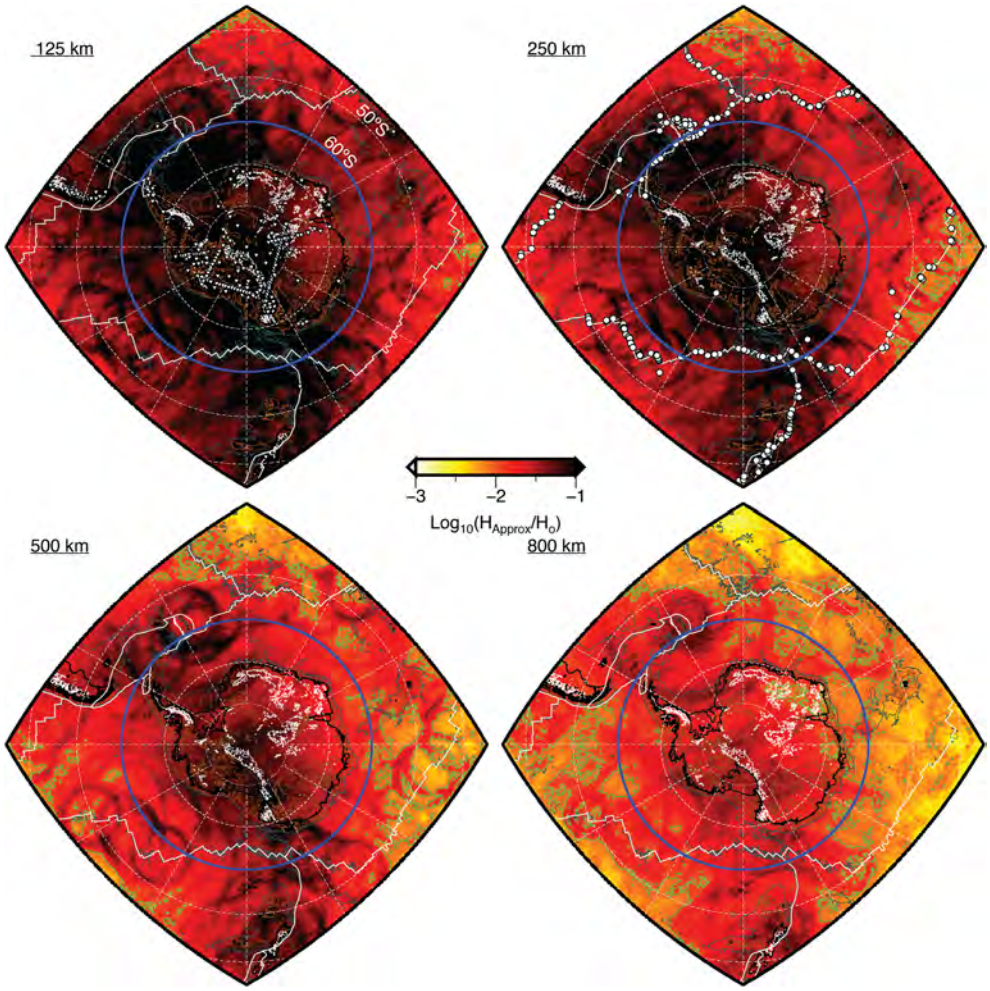

Figure 9. The approximate diagonal Hessian (equation (5)) used in the final model update is shown at 125-, 250-, 500-, and 800-km depth, and its variations serve as a proxy for relative data coverage. The thin green line denotes the −2 contour of $\mathrm{Log}_{10}(H_{\mathrm{approx}}/H_{\mathrm{o}})$. The blue line at 60°S denotes the northern boundary of the tomographic images shown in this study. The location of the broadband seismic stations (inverted triangles) and earthquakes (circles) are shown in the 125- and 250-km depth slices, respectively. Bathymetry, topography, plate boundaries, and lines of latitude and longitude are denoted similar to Figure 6.

previous two point-spread function tests. Images of the β_v component of the point-spread function (Figure 8) similarly indicate that the localized model perturbations are reasonably well preserved and also demonstrate distinct spatial variations in the curvature of the misfit function. For example, each region is characterized by differences in the strength of the misfit function's curvature, which is an intriguing observation, as well as varying degrees of vertical blurring. However, in all three instances variable lateral blurring is observed at depths shallower than 50 km, a region of the model we anticipate being less well resolved due to an absence of short (<25 s) period surface waves.

Beyond the results of the point-spread function tests, it is difficult to assess the reliability of ANT-20 elsewhere in the tomographic model, and thus, we must rely on other proxies (Bozdağ et al., 2016; Zhu et al., 2015). Equation (5), which approximates the diagonals of the Hessian matrix, is one such proxy that is diagnostic of the relative data coverage (Luo et al., 2013). The ability to resolve structure is directly dependent on data coverage, and in the case of adjoint tomography the degree of smoothing applied to the preconditioned kernels limits the length scales at which this structure may be resolved (Tape et al., 2007). Images of the approximate diagonals of the Hessian matrix (Figures 9, S3, and S4) suggest similar data coverage within the upper mantle south of 60°S, although slightly poorer coverage is suggested beneath some regions of

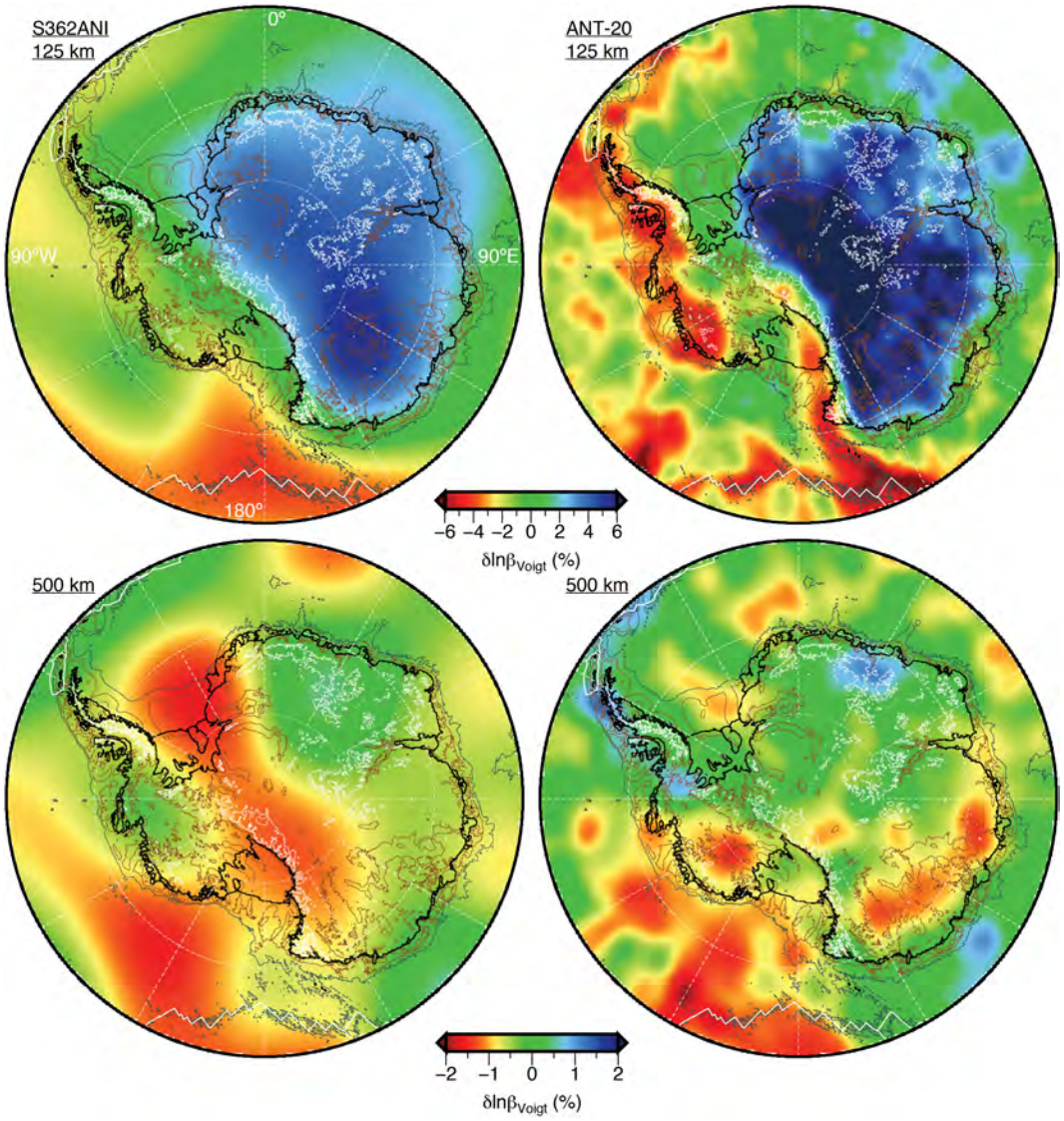

Figure 10. Comparisons of the Voigt average shear-wave speed structure of the starting model S362ANI (Kustowski et al., 2008) with that of ANT-20 at 125- and 500-km depths with respect to sea level. Mantle velocity anomalies are relative to the 1-D Earth model STW105 (Kustowski et al., 2008), which has been slightly modified to account for the topography of first- and second- order seismic discontinuities. Bathymetry and bedrock topography contours are shown for 1,000 m (thin white line) and −500 m (thin brown line), as well as −2,500 m (thin dark gray line) elevation in the oceans (Fretwell et al., 2013). Thicker white lines denote the plate boundaries (Bird, 2003), while dashed white lines denote lines of latitude every 10° or lines of longitude every 30°.

coastal East Antarctica. This includes the Lambert Graben, where weakening of the misfit function's curvature is observed in the point-spread function (Figure 8), suggesting perhaps slightly poorer resolution in this region, and thus a link between data coverage and resolution. Although this link cannot quantify the reliability of ANT-20, the similarity in relative data coverage (Figures 9, S3, and S4) combined with the geographic earthquake and station distribution (Figure 2) suggests that resolution throughout the upper mantle south of 60°S is likely similar to those regions probed by the point-spread function tests (Figures 6–8).

At transition zone depths relative data coverage begins to slowly decrease and may indicate poorer resolution. The potential inability of ANT-20 to resolve short-wavelength structures at these depths is countered by increasing the smoothing applied to the preconditioned kernels (section 3.4). Near 800-km depth data coverage rapidly deteriorates (Figures 9, S3, and S4) as does the reliability of the newly mapped features. Based on these observations, we only present and discuss ANT-20 south of 60°S and at depths shallower than 800 km.

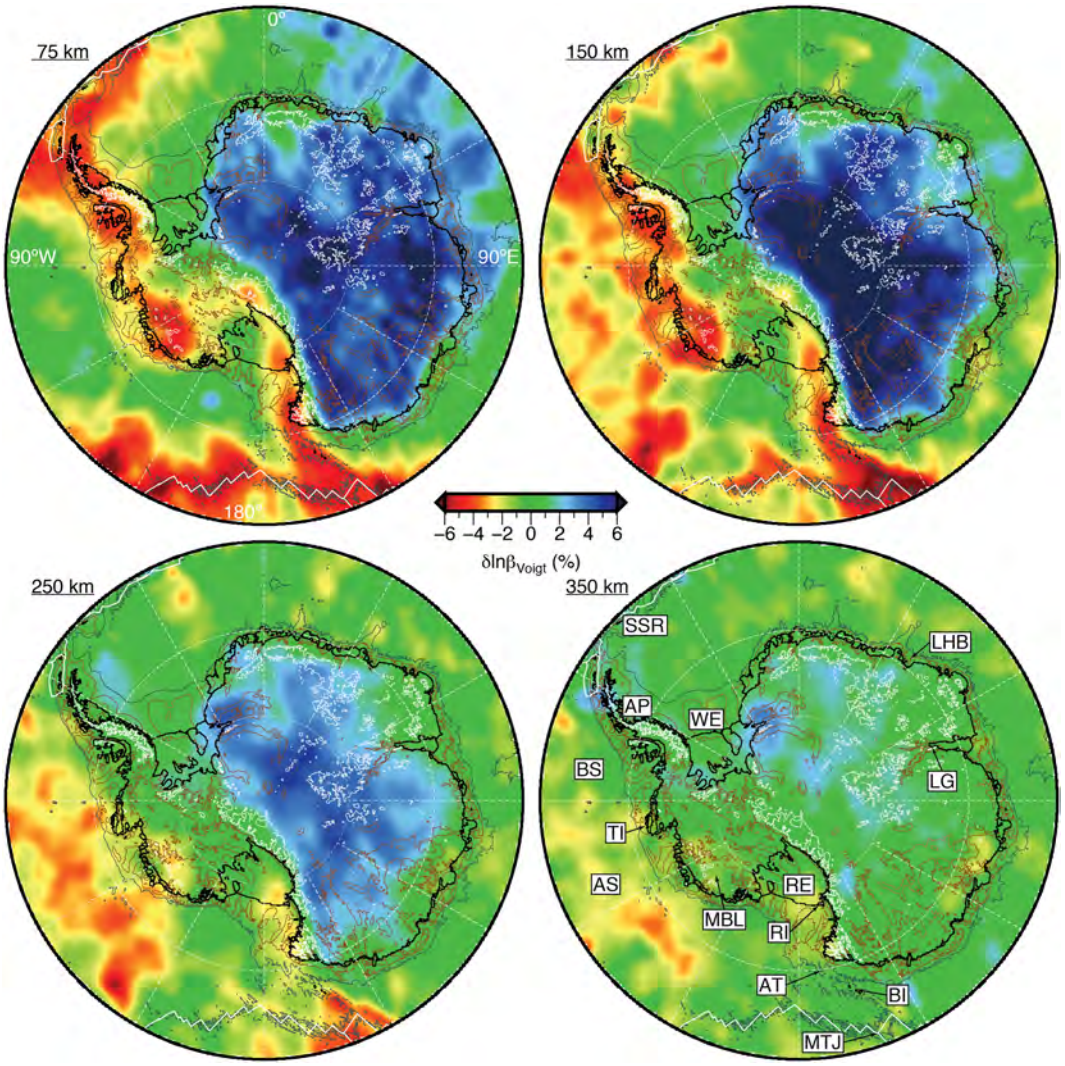

Figure 11. Tomographic images of the Voigt average shear-wave speed structure of ANT-20 at 75-, 150-, 250-, and 350-km depth with respect to sea level. Velocity anomalies, bathymetry, topography, plate boundaries, and lines of latitude and longitude are denoted as in Figure 10. Abbreviations: AT—Adare Trough, AS—Amundsen Sea, AP—Antarctic Peninsula, BI—Balleny Islands, BS—Bellingshausen Sea, LG—Lambert Graben, LHB—Lützow-Holm Bay, MTJ—Macquarie Triple Junction, MBL—Marie Byrd Land, RE—Ross Embayment, RI—Ross Island, SSR—South Scotia Ridge, TI—Thurston Island, WE—Weddell Embayment.

4.2. Voigt Average Shear-wave Speed Structure

The final seismic model obtained after 20 iterations, ANT-20, reveals strong short-wavelength heterogeneity within the Antarctic upper mantle and improved tomographic images of the transition zone compared to the starting model (Figure 10). Although c and η are also updated in the adjoint inversion, here we focus on the Voigt average shear-wave speed structure (Figures 10, 11, S5, and S6), which is calculated from β_v and β_h. Radial anisotropy can also be computed from β_v and β_h; however, given the imbalance in sensitivity of these two parameters (French & Romanowicz, 2014; Chang et al., 2015; Zhu et al., 2017), we refrain from interpreting the radial anisotropic structure at this time. To first order, the uppermost mantle is dominated by three prominent shear-wave speed anomalies that lie beneath East Antarctica, the northern West Antarctic Coast, and along the Transantarctic Mountains extending seaward (Figures 10, 11, S5, and S6). Within these features, the largest amplitude anomalies range from more than 8% faster than the reference model, STW105 (Kustowski et al., 2008), beneath East Antarctica, to slower than −6% in the vicinity of the Balleny Islands and the Macquarie Triple Junction. At greater depths, such as within the transition

zone, wave speed anomalies are between ±2%. We now briefly summarize a number of intriguing features observed in the tomographic images. The interpretation and implications of these features are discussed in section 5.

Tomographic images of the East Antarctic upper mantle reveal shear-wave speed anomalies that range from ~0% to greater than 8% (Figures 10, 11, S5, and S6). Wave speed anomalies faster than 2%, relative to the reference model, are largely confined to depths shallower than 300–350 km within the East Antarctic subcontinent, except at shallow (<100 km) depths where they extend beneath juxtaposed regions of relatively ancient oceanic lithosphere. The depth extent of the fast wave speed anomalies is not uniform and ranges from 250- to 350-km beneath the East Antarctic interior to 100–150 km along portions of the East Antarctic coast. In most instances, the thinner regions are relatively limited, extending inland by at most ~200 km. However, beneath Enderby-Kemp Land a thinner layer of fast wave speeds is imaged over an expansive region that extends inland by ~700 km.

The boundary between East and West Antarctica is delineated at shallow mantle depths by a lateral shear-wave speed gradient that is strongest along the Transantarctic Mountains near the Ross Embayment and lessens toward the Weddell Embayment (Figures 10, 11, S5, and S6). In the vicinity of the Ross Embayment, this gradient is strengthened by a slow, −2 to −4%, wave speed anomaly that extends from the Macquarie Triple Junction to the Balleny Islands and the Adare Trough, beyond which it bends inland, roughly following the western edge of the Ross Embayment. The depth extent of this feature is variable, but it appears to be almost entirely confined to the upper mantle. The slow wave speed anomalies extend to 250–300-km depth in the Balleny Islands region, to 350–400-km depth in the northern Victoria Land sector of the Transantarctic Mountains, and to less than 200-km depth beneath the southern Transantarctic Mountains. At mantle depths shallower than 100 km, a weak slow (≈ −2%) wave speed anomaly extends from the southern Transantarctic Mountains, across the West Antarctic Rift System, and into Marie Byrd Land, where it connects to a large and geometrically complex shear-wave speed anomaly.

Along the Bellingshausen and Amundsen Sea Coasts, a prominent slow (<−2%) shear-wave speed anomaly extends from Marie Byrd Land, through the Antarctic Peninsula, and then bends east following the South Scotia Ridge (Figures 10, 11, S5, and S6). At depths shallower than 100 km, this anomaly is confined inboard of the continental shelf until reaching the northern half of the Antarctic Peninsula, which is juxtaposed by relatively young oceanic lithosphere originating from the ancestral Phoenix-Antarctic spreading center in the Bellingshausen Sea. Much of this anomaly extends no deeper than 200–250-km depth. However, beneath Marie Byrd Land and the adjacent regions of the West Antarctic Rift System slow wave speeds extend down from the upper mantle, through the transition zone, and into the lower mantle. Intriguingly, the slow wave speed anomalies beneath Marie Byrd Land and the Amundsen Sea Coast also appear to be linked to a broad region of slow shear wave speeds offshore beneath the Bellingshausen and Amundsen Seas that extends into the deeper mantle (Figures 10, 11, S5, and S6).

4.3. A Comparison With Previous Tomographic Studies

Since pioneering surface wave studies of the Antarctic upper mantle have revealed the strong seismic dichotomy of the east and west subcontinents (e.g.,Danesi & Morelli, 2001 ; Ritzwoller et al., 2001), only a few models have attempted regional tomographic inversions that span the entire continent (e.g., An et al., 2015a). Therefore, seismological constraints across the Antarctic are, in part, obtained from global tomographic models. Despite recent models being generally consistent worldwide (Lekic et al., 2012), they still suggest vastly different structure beneath Antarctica (Figure 12; e.g., Ritsema et al., 2011; French et al., 2013; Schaeffer & Lebedev, 2013). For example, at 100-km depth, S40RTS (Ritsema et al., 2011) depicts shear-wave speed anomalies no faster than ~2% beneath East Antarctica and near the 1-D global average beneath West Antarctica. At the same depth, models like SEMUM-2 (French et al., 2013) and SL2013sv (Schaeffer & Lebedev, 2015), which utilize additional Antarctic seismic data, reveal anomalies with amplitudes similar to the pioneering continental-scale surface wave studies conducted more than 15 years ago (e.g., Danesi & Morelli, 2001; Ritzwoller et al., 2001) and begin to just hint at second-order features that are well resolved in regional studies (e.g., Brenn et al., 2017; Graw et al., 2016; Lloyd et al., 2013, 2015; Shen, Wiens, Anandakrishnan et al., 2018; Watson et al., 2006).

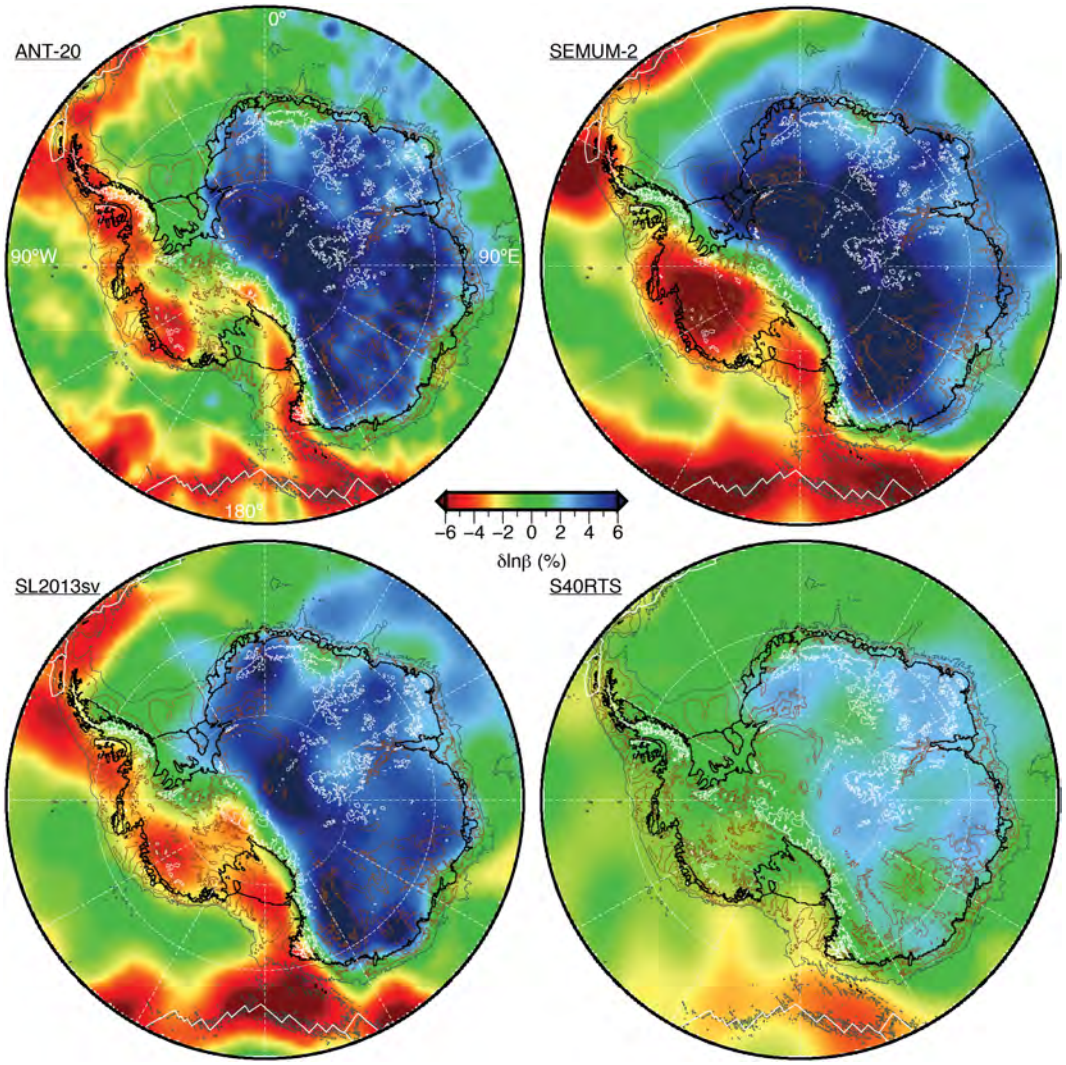

Figure 12. A comparison of ANT-20 with other recent global shear-wave speed models at 100-km depth. ANT-20 and SEMUM-2 (French et al., 2013) show Voigt average shear-wave speed anomalies, while SL2013sv (Schaeffer & Lebedev, 2013) and S40RTS (Ritsema et al., 2011) depict vertically polarized shear-wave speed anomalies. Bathymetry, topography, plate boundaries, and lines of latitude and longitude are denoted as in Figure 10.

These emerging features include prominent slow shear-wave speeds beneath portions of West Antarctica and the Ross Embayment and evidence of seismic heterogeneity beneath East Antarctica (Figure 12). Relative to global models, ANT-20 provides significantly enhanced tomographic images, revealing that the slowest West Antarctic shear-wave speeds are concentrated beneath Marie Byrd Land and are limited in their extent beneath the adjacent subglacial basins of the West Antarctic Rift System. Regional studies (Lloyd et al., 2015; Shen, Wiens, Anandakrishnan et al., 2018) report similar findings and also differentiate the Ellsworth-Whitmore mountains crustal block, as does ANT-20. Likewise, in the Ross Embayment, ANT-20 images the slowest regional wave speeds along and in places beneath the Transantarctic Mountains, while revealing moderate anomalies beneath the eastern basins of the Ross Embayment, consistent with a number of regional studies (Brenn et al., 2017; Graw et al., 2016; Heeszel et al., 2016; Shen, Wiens, Anandakrishnan et al., 2018; Watson et al., 2006). Finally, ANT-20 exhibits greater seismic heterogeneity beneath East Antarctica, but it is the sharp boundaries of the fast upper mantle anomalies that are most striking in comparison to the smoother global tomographic models.

For example, at 100 km depth vertically polarized shear-wave speeds in ANT-20 are on average ~0.09 km/s (~2%) faster than those reported by Shen, Wiens, Anandakrishnan et al. (2018) but are on average

~0.02 km/s(~0.4%) slower than in O'Donnell et al. (2019) (Figure S7). Understanding these differences is important, as studies of solid Earth and cryosphere interactions are now merging multiple tomographic models to constrain solid Earth properties. While differences among models are related to the parameterization and regularization of the inversion, differences in average wave speed often arise from the effect of anelasticity. Because anelasticity causes physical dispersion of seismic waves and, thus, seismic wave speeds are frequency dependent, a reference frequency is chosen (conventionally 1 Hz) or implied by the frequency content of the seismic observations. The latter is the case for many Antarctic studies, including An et al. (2015a), Graw et al. (2016), and Heeszel et al. (2013, 2016), who forgo the needed anelastic correction to obtain 1 Hz wave speeds. Some recent Antarctic studies do account for anelasticity and report 1 Hz wave speeds assuming either constant attenuation in the upper mantle ($Q\mu = 150$; Shen, Wiens, Anandakrishnan et al., 2018) or the PREM 1-D attenuation model ($Q\mu = 80$ at 100 km depth; O'Donnell et al., 2019). ANT-20 presents 1 Hz wave speeds based on the attenuation model QL6 ($Q\mu = 70$ at 100 km depth; Durek & Ekström, 1996). Shen, Wiens, Anandakrishnan et al. (2018) report that using an upper mantle $Q\mu$ of 70 increases wave speeds by ~1% and thus reduces the average difference between their model and ANT-20 to ~1% (0.045 km/s at 100 km depth). Thus, the average wave speed difference between ANT-20 and these other studies is within reported uncertainties (0.05–0.065 km/s, Shen, Wiens, Anandakrishnan et al., 2018; 0.02–0.05 km/s, O'Donnell et al., 2019) when attenuation is considered. This comparison demonstrates the importance of correcting wave speeds to the same reference frequency using the same attenuation structure prior to merging or comparing tomographic models.

5. Discussion

5.1. Implications for the Structure of East Antarctica

Much of East Antarctica is underlain by fast shear-wave speed anomalies that extend to 250–350-km depth beneath the East Antarctic interior and to 100–150-km depth along the East Antarctic coast (Figures 10, 11, S5, S6, and 13). These anomalies are the manifestations of cold thick lithospheric roots that are characteristic of cratons and Proterozoic fold belts (Grand & Helmberger, 1984; Jordan, 1975). The depth extent and magnitude of these fast wave speed anomalies can provide a measure of the relative thickness of the lithosphere. Thus, our tomographic images suggest thicker lithosphere within the interior of East Antarctica and thinner lithosphere along the East Antarctica coast. Thinner lithosphere is perhaps expected along the coast, as it is a former rifted margin from the Jurassic/Cretaceous breakup of Gondwana (Boger, 2011). In most regions, the thinner lithosphere extends inland by less than ~200 km, but to some extent the thinner coastal lithosphere may be an artifact of the natural smoothing of the tomography. In contrast to the rest of East Antarctica, much greater variability in lithospheric thickness, as well as structure, is found stretching from western Dronning Maud Land to the Lambert Graben. This includes a broad region of inferred thinner lithosphere beneath Enderby-Kemp Land that extends inland several hundred kilometers from the coast, as well as a region of distinctly average upper mantle wave speeds beneath Fimbulheimen in Dronning Maud Land (Figure 13).

Although the amplitude of the fast shear-wave speed anomalies beneath East Antarctica may exceed 8%, they more commonly range from 2% to 6%. This is consistent with global observations of shear-wave speed anomalies within the lithosphere of cratons and Proterozoic fold belts, which are between 5–6% and 2–3%, respectively (Lebedev et al., 2009). The tomographic images indicate that cratonic-like fast (>5%) wave speed anomalies are observed beneath central East Antarctica and the deep subglacial basins of Wilkes Land (Figure 13). The thick lithosphere and extremely fast velocities beneath the Gamburtsev Subglacial Mountains are consistent with Heeszel et al. (2013), who showed that Rayleigh wave phase velocity curves in this region are most compatible with Archean or Early Proterozoic cratonic lithosphere worldwide. In contrast, only moderately fast (<5%) wave speed anomalies are imaged beneath Dronning Maud Land and Enderby-Kemp Land, where greater variability in lithospheric thickness is also suggested. Thus, there is a striking dichotomy between extremely thick and fast continental lithosphere beneath central Antarctica and the subglacial basins that originally rifted from Australia, versus the thinner and more variable lithosphere characterized by modest wave speed anomalies beneath Donning Maud Land and adjoining regions of Indian and African affinity.

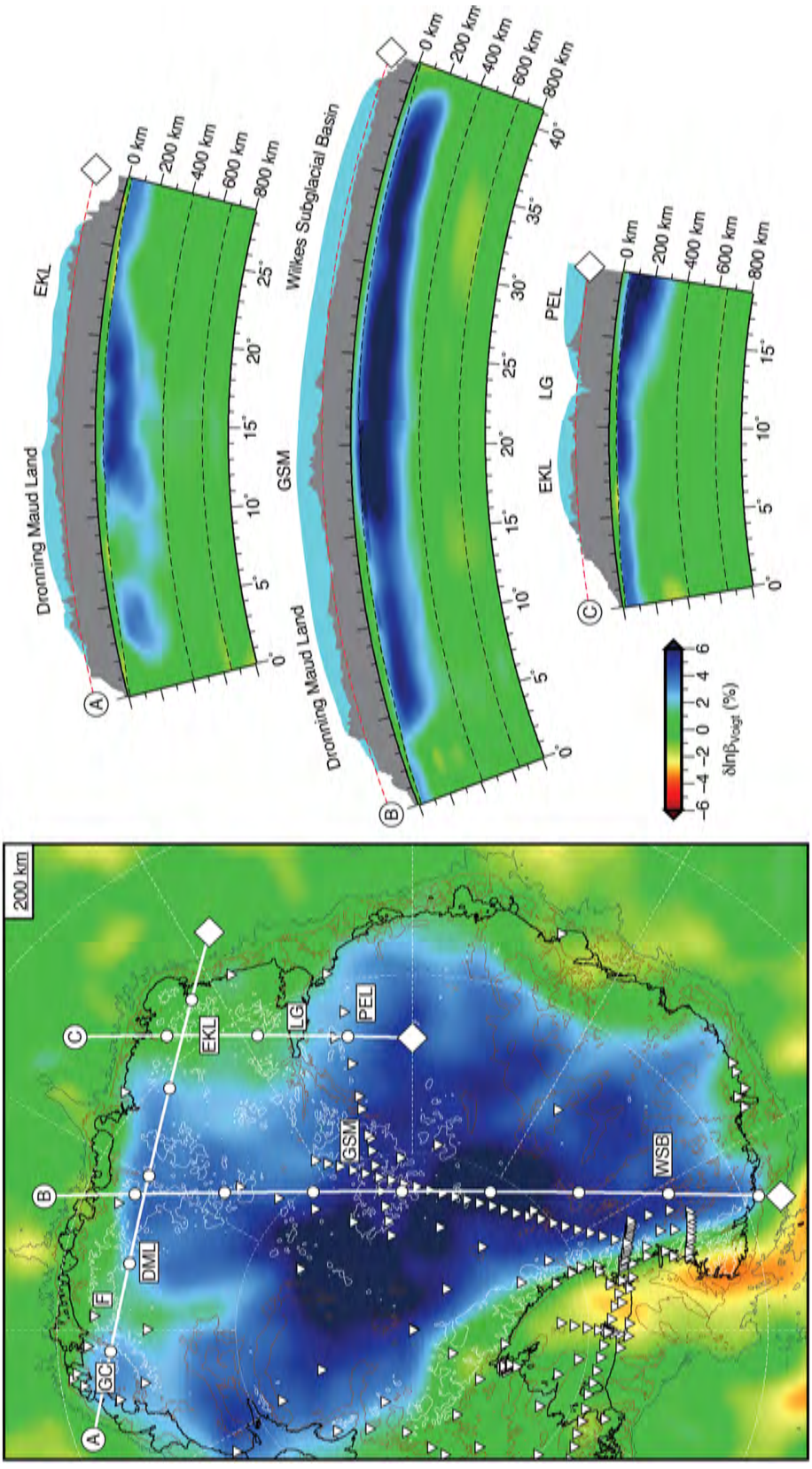

Figure 13. Expanded image of the Voigt average shear-wave speed structure beneath East Antarctica at 200-km depth and along profiles A, B, and C. The horizontal slice shows the broadband seismic stations (inverted triangles) used in this study and the paths of profiles A, B, and C. These paths are depicted in the horizontal slice as thick white lines that begin at a large white circle and end at a large white diamond. Along each path smaller white circles mark every 5°. Finally, the shear-wave speeds, bedrock topography, bathymetry, plate boundaries, and lines of latitude and longitude are denoted as in Figure 10. The particulars of the vertical slices are similar to Figure 6. Abbreviations: DML—Dronning Maud Land, EKL—Enderby-Kemp Land, F—Fimbulheimen, GSM—Gamburtsev Subglacial Mountains, GC—Grunehogna Craton, LG—Lambert Graben, PEL—Princess Elizabeth Land, WSB—Wilkes Subglacial Basin.

It is noteworthy that regions of high modal deglaciated elevation, such as Enderby-Kemp Land, are ~700–800 m higher than the deep subglacial basins of Wilkes Land, despite both regions possessing similar crustal thicknesses of ~40 km (O'Donnell & Nyblade, 2014). Therefore, the warmer geotherm of Enderby-Kemp Land, suggested by our tomographic images, implies the existence of less dense mantle material that could, in part, provide support for the elevated topography of the region.

The uppermost mantle beneath Fimbulheimen is characterized by an absence of fast (>2%) shear-wave speeds (Figures 10, 11, S5, S6, and 13). These near average wave speeds are inconsistent with a region that coalesced during or prior to the Neoproterozoic(e.g., Lebedev et al., 2009), suggesting delamination of what must have been Precambrian age lithosphere. Unlike the southern Transantarctic Mountains (Shen, Wiens, Stern et al., 2018), no shallow slow wave speed anomaly is observed. Thus, we suggest that the asthenosphere, which flowed in above the foundered lithosphere, has already cooled, suggesting delamination occurred prior to the Cenozoic. Possible times consistent with geologic studies include the Late Cambrian or Mid-Jurassic. Jacobs et al. (2008) suggested a delamination event occurring at ~500 Ma in order to explain the late-tectonic granitoid intrusions found in Dronning Maud Land. Alternatively, within this region of Dronning Maud Land, there exists remnants of mid-Jurassic flood basalts associated with the Karoo plume, which are estimated to have originally been as much as 2-km thick (Sirevaag et al., 2018). The impingement of the Karoo plume beneath this sector may have thermally and chemically modified the overlying lithosphere, triggering destabilization of the lithosphere. A similar plume-triggered delamination event has been proposed for the Yellowstone hot spot based on geological studies of the Columbia River flood basalts (Camp & Hanan, 2008). Finally, the tomographic images are unable to differentiate between these events, and thus either or both are possible.

5.2. Mantle Velocity Anomalies and the Tectonics of West Antarctica

West Antarctica contains several prominent slow shear-wave speed anomalies. One of the largest and strongest anomalies is located beneath eastern Marie Byrd Land, centered near Mt. Sidley in the Executive Committee Range (Figures 10, 11, S5, S6, and 14). Marie Byrd Land consists of a topographic dome and several prominent volcanic systems characterized by recent volcanic or ongoing magmatic activity (LeMasurier, 1990; Lough et al., 2013; Panter et al., 1994; Wilch et al., 1999). The pattern of the slow wave speed anomalies beneath Marie Byrd Land correlates well with long-wavelength elevated topography that is not isostatically supported by the crust (Chaput et al., 2014). This fact, along with the active magmatism, suggests that both the high elevation and volcanism result from elevated upper mantle temperatures (Hansen et al., 2014; Lloyd et al., 2015). The anomaly has a large geographical extent (~1,000 km) and amplitude (~−4 to −6%) between depths of about 75–250 km. At greater depths, the anomaly's amplitude is reduced and moves somewhat further south but remains visible within the transition zone (Figure 13). Poor resolution at depths greater than 800 km prevents determining whether this feature represents a plume originating in the lower mantle or a thermal anomaly restricted to the transition zone and shallower depths.

Previous studies have attempted to image the configuration of the Marie Byrd Land anomaly in the transition zone. Hansen et al. (2014) detected slow wave speed anomalies in the transition zone beneath Marie Byrd Land and suggested that this anomaly extended into the transition zone, but the anomalies were not well localized. Emry et al. (2015) investigated the thickness of the transition zone as a proxy for temperature, as the transition zone should be thinner in hot regions. They found evidence for higher temperatures beneath the northeast coast of Marie Byrd Land and also along the southern edge of West Antarctica, but not beneath central Marie Byrd Land. In contrast, the images here show significant slow anomalies beneath central West Antarctica not far from the Marie Byrd Land dome, suggesting that the Marie Byrd Land thermal anomalies in the upper mantle are linked to thermal anomalies in similar locations within the transition zone. Thus, the slow shear wave speed anomalies beneath Marie Byrd Land are consistent with the presence of a mantle plume, as suggested by some studies (Behrendt, 1999; LeMasurier & Landis, 1996). A comparison of recent global-scale tomographic inversions with deeper resolution than ANT-20 also generally supports slow wave speed structure through and below the transition zone in the Marie Byrd Land region (Phillips et al., 2018).

The Marie Byrd Land slow shear-wave speed anomaly is linked at shallow depths to a continuous band of slow wave speeds extending along the West Antarctic coast from Marie Byrd Land through the Amundsen Sea Embayment to the Antarctic Peninsula (Figures 10, 11, S5, S6, and 14). In contrast to the

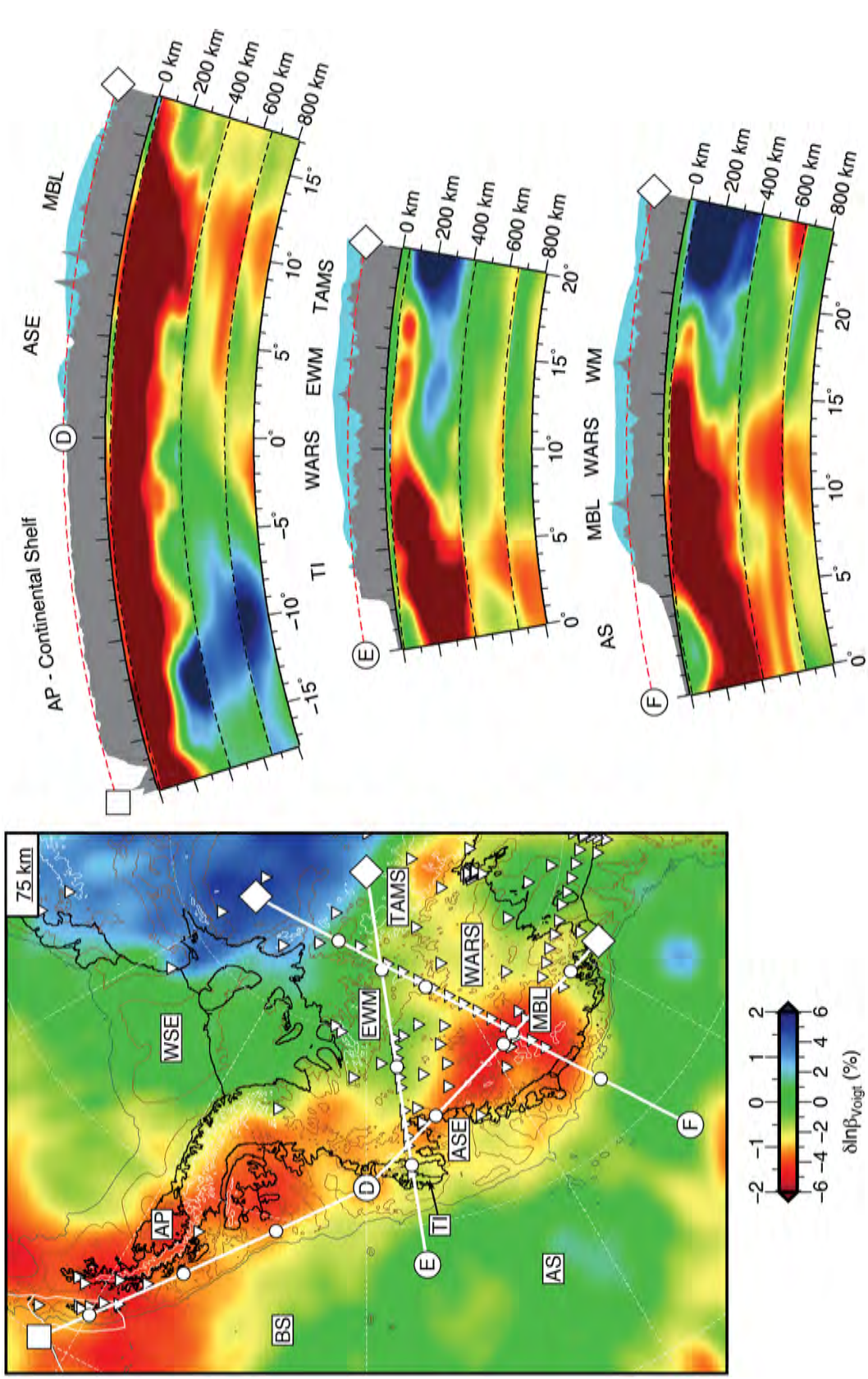

Figure 14. Expanded image of the Voigt average shear-wave speed structure beneath West Antarctica at 75-km depth and along profiles D, E, and F. The shear-wave speed structure in the horizontal and vertical slices range from ±6% and ±2%, respectively. The horizontal slice depicts the locations of the profiles, shear-wave speeds, bedrock topography, bathymetry, plate boundaries, and lines of latitude and longitude similar to Figure 13. Meanwhile, the particulars of the vertical slices are similar to Figure 6. Abbreviations: AS—Amundsen Sea, ASE—Amundsen Sea Embayment, AP—Antarctic Peninsula, BS—Bellingshausen Sea, EWM—Ellsworth-Whitmore Mountains, MBL—Marie Byrd Land, TAMS—Transantarctic Mountains, TI—Thurston Island, WARS—West Antarctic Rift System, WSE—Weddell Sea Embayment, WM—Whitmore Mountains.

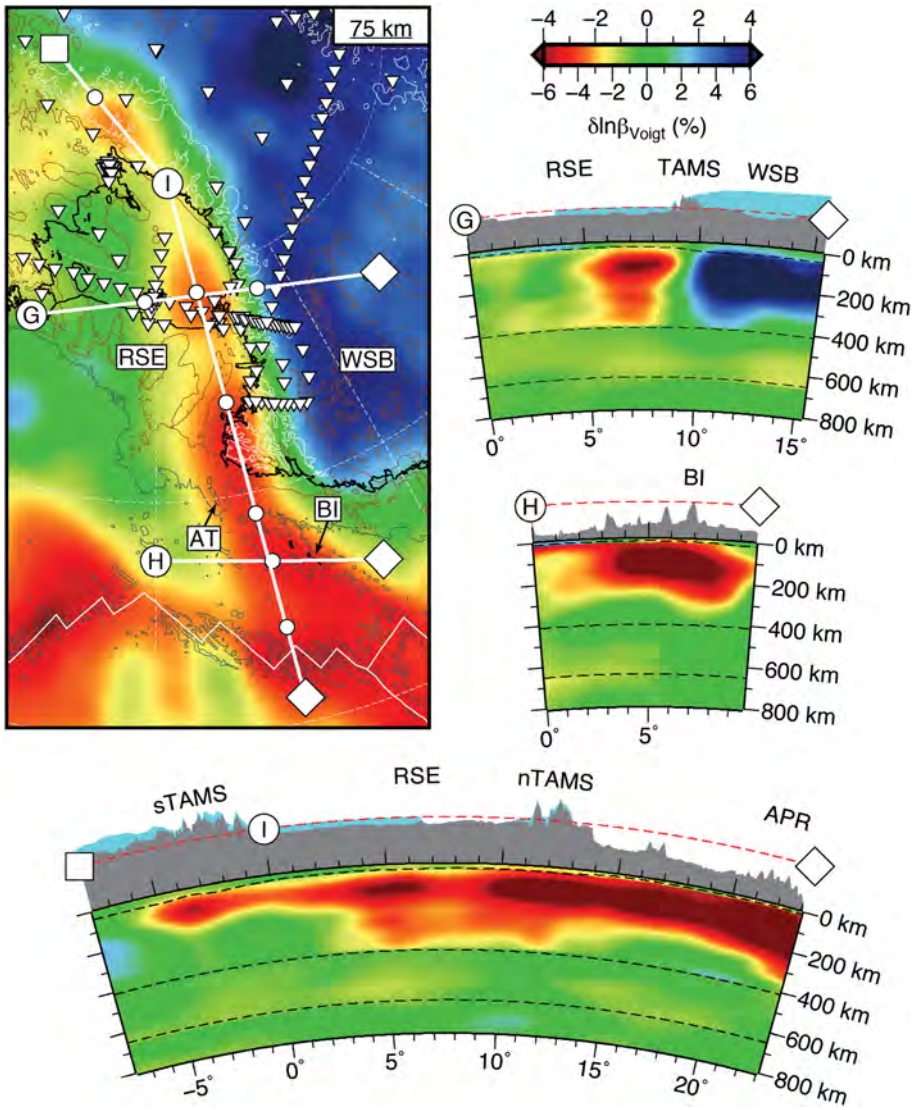

Figure 15. Expanded image of the Voigt average shear wave speed structure beneath the Ross Sea Embayment at 75-km depth and along profiles G, H, and I. Note that the shear-wave speeds range from ±6% and ±4% in the horizontal and vertical slices, respectively. The horizontal slice depicts the locations of the profiles, shear-wave speeds, bedrock topography, bathymetry, plate boundaries, and lines of latitude and longitude similar to Figure 13. Meanwhile, the particulars of the vertical slices are similar to Figure 6. Abbreviations: APR—Antarctic-Pacific Ridge, AT—Adare Trough, BI—Balleny Islands, RSE—Ross Sea Embayment, (*n*, *s*)TAMS—(northern, southern) Transantarctic Mountains, WSB—Wilkes Subglacial Basin.

Marie Byrd Land anomaly, this slow anomaly becomes much weaker below 200-km depth and is replaced by fast wave speeds beneath the Antarctic Peninsula. In addition, profiles normal to the coast near Marie Byrd Land and the Amundsen Sea Embayment (Figure 14), show that the shallow coastal wave speed anomalies are connected to a broad slow anomaly at greater depths (beginning at ~250 km) beneath old oceanic lithosphere that formed following the separation of Zealandia and Antarctica around 90 Ma (Eagles et al., 2004). The slow upper mantle wave speeds are consistent with recent volcanism, both onshore along the Amundsen Sea Embayment (Corr & Vaughan, 2008) and at Peter I Island (Kipf et al., 2014), and with anomalously elevated bathymetry in the oceanic regions (Wobbe et al., 2014). This feature offshore of the Amundsen Sea Embayment can be attributed to upper mantle thermal anomalies near the region where spreading originated between Zealandia and Antarctica, in which the initiation of spreading has been attributed to a mantle plume (Weaver et al., 1994). Because shallower slow wave speeds along the coastline are

connected to both the deep anomaly offshore and the Marie Byrd Land anomaly they may be influenced by both sources.

Beneath the Antarctic Peninsula slow wave speeds are limited to depths shallower than ~200 km and are underlain by fast seismic anomalies towards the end of the Peninsula (Figures 10, 11, S5, S6, and 14). We interpret this structural pattern in term of the Cenozoic subduction history of the Phoenix plate along this margin. Although subduction of the Phoenix plate beneath the Antarctic Peninsula throughout the Mesozoic, subduction sequentially ceased from southwest to northeast during the Cenozoic as ridge segments of the Phoenix-Antarctic ridge were subducted beneath the Antarctic Peninsula (Eagles et al., 2004, 2009; Larter et al., 1997). Thus, leading to the formation of a slab window that started near the southernmost base of the Antarctic Peninsula at ~61 Ma and grew along the Peninsula until significant subduction of the remnant Phoenix plate ceased beneath the South Shetland Islands at 3.3 Ma (Eagles, 2004). Slab windows observed elsewhere in the world are accompanied by the destruction of the overriding plate's lithosphere and its replacement by warm, slow wave speeds (Russo et al., 2010), as predicted by geodynamic models (Groome & Thorkelson, 2009). We propose that the subduction of the Phoenix-Antarctic spreading center destroyed the continental lithosphere along the Pacific coast of the Antarctic Peninsula and replaced it with hot, slow wave speed mantle. The time elapsed since this activity (<60 Ma) is insufficient to form new lithosphere and to significantly cool the infilled asthenosphere, thus the thermal anomaly formed by ridge subduction remains in the upper mantle along the western side of the Antarctic Peninsula. Fast velocity anomalies at depths from 300 to 700 km below the Antarctic Peninsula are likely remnants of the subducted Phoenix plate.

Near-average mantle wave speeds dominate at most depths beneath inland region of West Antarctica (Figures 10, 11, S5, S6, and 14). This suggests an absence of major large-scale thermal anomalies and is generally consistent with previous studies suggesting a modest thickness of cold lithosphere in this region (Heeszel et al., 2016; Shen, Wiens, Anandakrishnan, et al., 2018). It is also broadly consistent with geologic evidence suggesting that most of the West Antarctic Rift System's extension occurred in the Cretaceous and early Cenozoic (Siddoway, 2008; Wilson & Luyendyk, 2009), although spatially restricted rifts with lesser amounts of extension may have been active more recently (Granot et al., 2010; Lloyd et al., 2015). Near-average mantle velocities also characterize the Ronne Ice Shelf region, which is consistent with a Mesozoic origin of extended crust in this area (Jordan et al., 2013).

5.3. A Continuous Mantle Seismic Anomaly From the Balleny Islands to the Transantarctic Mountain Front

A striking feature of the uppermost mantle image is a band of slow shear-wave speeds extending from the southeast Indian and Pacific-Antarctic spreading centers at the Macquarie Triple Junction, through the volcanic Balleny Islands, the extinct Adare Trough spreading center, and along the front of the Transantarctic Mountains (Figures 10, 11, S5, S6, and 15). This pattern provides important evidence linking the tectonic development of the Transantarctic Mountains with Cenozoic plate tectonic and geodynamic processes offshore.

The Balleny Islands lie between the currently active spreading centers of the Macquarie Triple Junction and the extinct Adare Trough spreading center. Although remote and little studied, the volcanism of the Balleny Islands contains a HIMU signature (Berg et al., 1997), and they have been associated with a mantle plume based on the upper and middle mantle slow wave speed anomalies (Zhao, 2007). However, in this region slow wave speeds are not imaged at depths greater than 250 km in this study (Figures 10, 11, S5, S6, and 15). The Adare Trough is located just north of the Ross Embayment and near the northern terminus of the Transantarctic Mountains, and it displays magnetic anomalies resulting from sea floor spreading from 46 to 26 Ma (Cande et al., 2000; Granot et al., 2013), with slow spreading continuing to 11 Ma and evidence of some extensional faulting up to the present (Granot et al., 2010; Granot & Dyment, 2018). The slow wave speeds observed in this region show that the upper mantle retains the signature of an extensional tectonic environment despite the fact that plate tectonic motion along this boundary has ceased.

The slow shear-wave speed anomaly continues southward along the western margin of the Ross Embayment to the southern Transantarctic Mountains (Figure 15). The Ross Embayment formed through a series of extensional events beginning in the Cretaceous (Luyendyk et al., 2003; Siddoway, 2008) and continued

through Terror Rift extension from the mid-Miocene to recent (Henrys et al., 2008; Fielding et al., 2008). The initial stages of rifting affected Marie Byrd Land and the eastern Ross Embayment, whereas later stages were narrowly concentrated along the western margin of the Ross Embayment adjacent to the Transantarctic Mountains (Wilson & Luyendyk, 2009). The upper mantle seismic structure reflects this history, as the recently active western side of the Ross Embayment shows much slower wave speeds than the long dormant eastern side. This pattern is in agreement with upper mantle structure imaged by other tomographic studies (e.g., Heeszel et al., 2016; Shen, Wiens, Anandakrishnan et al., 2018; White-Gaynor et al., 2019).

The upper mantle structure along the western and southern boundary of the Ross Embayment shows three prominent higher amplitude anomalies. These anomalies located beneath the Hallet Volcanic Zone, the Mt. Erebus and Terror Rift region, and the southern Transantarctic Mountains, are all located beneath regions of mid-to-late Cenozoic volcanism (Figure 15). In general, where this anomaly extends beneath the Transantarctic Mountains, the region is characterized by greater width and elevation. The slow wave speed anomaly is much narrower and less pronounced in the central Transantarctic Mountains where the mountains are narrower, lacking volcanism, and where the cold continental lithosphere extends up to the Transantarctic Mountains front (Wannamaker et al., 2017). Thus, the width and amplitude of the upper mantle slow wave speed anomaly adjacent to the Transantarctic Mountains front correlates well with the broad-scale structural and tectonic variation along the front, as also discussed in Graw et al. (2016), Brenn et al. (2017), and Shen, Wiens, Stern et al. (2018). Here, we discuss each of these regions individually.

The slow wave speed anomaly is broad beneath the Hallett Volcanic Zone, along the northwestern boundary between the Ross Embayment and East Antarctica. The region around the Hallett Volcanic Zone shows volcanism dating from at various times between 48 and 1 Ma (Mortimer et al., 2007; Rocchi et al., 2002). The geochemistry of the lavas has an ocean island basalt affinity, similar to other volcanoes in the Balleny Islands and in the Erebus Volcanic Province to the north and south, respectively. Thus, the slow upper mantle wave speeds spatially align with Neogene volcanism and are consistent with thin lithosphere as well as the presence of warm mantle that may contain partial melt. Graw et al. (2016) and Brenn et al. (2017) also find slow upper mantle wave speeds along the northwestern margin of the Ross Embayment and interpreted them as the signature of rift-related decompression melting.

The Mt. Erebus region comprises several large volcanic systems and the Terror Rift, which has undergone 15 km of extension from 17 Ma to recent (Henrys et al., 2008). Detailed body and surface wave tomography using temporary seismic stations in this region shows a sharp boundary between slow and fast upper mantle near the crest of the Transantarctic Mountains (Brenn et al., 2017; Graw et al., 2016; Lawrence et al., 2006a, 2006b; Watson et al., 2006), in agreement with the present study. The slow wave speeds in this region are consistent with the general absence of lithosphere and high upper mantle temperatures expected beneath a recently extending rift zone with a small amount of continuing decompression melting. There has been considerable discussion about the origin of Mt. Erebus volcanics, with some proposing a deep mantle plume source based on geochemical studies (Kyle et al., 1992; Phillips et al., 2018), whereas other investigations suggest that rift-related decompression melting is a better explanation (Cooper et al., 2007). Figures 10, 11, S5, S6, and 15 show that the Erebus region is underlain by slow wave speeds throughout the upper mantle, but with little to no evidence of a significant slow wave speed signature in the transition zone. Global tomography (e.g., French et al., 2013) reveals additional slow wave speeds in the region to depths of ~1,000 km, but no evidence of a deeper slow wave speed structure. This leaves the results inconclusive about the possible plume origin of Mt. Erebus and surrounding volcanoes.

The tomographic images (Figures 10, 11, S5, S6, and 15) indicate lower amplitude slow- wave speeds to the south of Mt. Erebus, but the amplitude of the slow anomalies again increase beneath the southern Transantarctic Mountains. This is the only location along the Transantarctic Mountains front where Cenozoic volcanism occurs on the East Antarctic side of the mountain range, at Mt. Early (Stump et al., 1980) and where Cenozoic volcanic rocks are found in moraine deposits (Licht et al., 2018). Previous studies show that the lithospheric mantle is missing beneath the southern Transantarctic Mountains and has been replaced by warm asthenosphere that reaches very close to the Moho (Heeszel et al., 2016; Shen, Wiens, Stern, et al., 2018). This study provides superior structural resolution at greater depths, thus confirming that this mantle anomaly is caused by missing lithosphere and that it is confined to depths shallower than 150 km, as would be expected for an anomaly caused by lithospheric delamination.

Overall, the slow shear-wave speed anomaly extending from the Macquarie Triple Junction to the southern Transantarctic Mountains connects multiple regions of late Cenozoic extension and volcanism. It most likely marks the trace of late Cenozoic extensional tectonics, with mantle temperatures remaining elevated after cessation of lithospheric thinning. Where this former plate boundary traverses the Antarctic continent, it supplies additional buoyancy and is accompanied in some places by lithospheric destruction, creating broad regions of elevated topography.

6. Summary and Conclusions

We use adjoint tomography (e.g., Tape et al., 2007; Tromp et al., 2005; Zhu et al., 2015) along with a growing Antarctic broadband seismic data set (Figure 2 and Table S1) to seismically image the upper mantle and transition zone beneath Antarctica and portions of the southern midlatitude oceans. This new tomographic model, ANT-20, assumes a radially anisotropic mantle and is constructed from observations of three-component waveforms containing *P*, *S*, Rayleigh, and Love waves, including reflections and overtones, from 270 earthquakes recorded by 323 seismic stations (Figure 2). Although c and η are imaged by the inversion and ρ is scaled based on equation (1), herein we present and discuss the high-resolution images of the Voigt average shear-wave speed structure of ANT-20 (Figures 10–15 and S5–S7). Assessing the resolution and quality of ANT-20 is challenging, but a series of point-spread function tests (Figures 6–8) along with a proxy for data coverage (Figure 9) suggest that structure is reliably resolved south of 60°S latitude and within the mantle at depths shallower than 800 km (section 4.1). Within this region, ANT-20 is a significant improvement over global and continental-scale tomography models (Figures 10 and 12) and it approaches the level of resolution obtained by spatially limited regional studies (section 4.3 and Figure S7).

Our new tomographic images reveal variable lithospheric thickness across East Antarctica and a region of possible lithospheric destruction beneath Fimbulheimen in Dronning Maud Land (Section 5.1; Figure 13). We suggest that the lithosphere in this region delaminated either during the Early Paleozoic (Jacobs et al., 2008) or the mid-Jurassic due to the Karoo plume. We also image pronounced slowshear-wave speed anomalies along the Transantarctic Mountain front, which extend seaward beneath the Adare Trough and the Balleny Islands, connecting with the Macquarie Triple Junction (Section 5.3; Figure 15). Another band of slow wave speeds are observed beneath Marie Byrd Land, extending along the coast and through the Antarctic Peninsula (Section 5.2; Figure 14). Beneath Marie Byrd Land, this anomaly extends into the transition zone, possibly indicating the presence of a mantle plume, whereas elsewhere, it is mostly confined to depth shallower than 250 km. Along the Antarctic Peninsula, we interpret these slow wave speeds to reflect a slab window that formed as subduction ceased northeastward in the Cenozoic. In addition, beneath the northern part of the Antarctic Peninsula, we find fast wave speeds consistent with the subducted Phoenix plate. Finally, the slow wave speed anomalies beneath the Amundsen Sea coast are connected to deeper anomalies offshore, suggesting a connection to a deeper mantle process.

Acknowledgments
We thank the many individuals and organizations who have helped with the installation, maintenance, and sadly in some instances the demobilization of 297 remote Antarctic broadband seismic stations used in this study. Although Table S1 lists all stations and their respective data repositories, we particularly wish to thank Timo Tiira, Alfons Eckstaller, Thierry Camelbeeck, and Meijan An for their help in obtaining three-component earthquake seismograms from a number of broadband seismic stations along coastal East Antarctica. Andrew J. Lloyd and Douglas A. Wiens were supported by NSF Grants PLR-1142518, PLR-1246712, and OPP-1744883. Support has also come from NASA Sea-level Change Team ROSES Grant 105393-281945.02.53.03.15. A portion of this researchwas carried out at the Jet Propulsion Laboratory, California Institute ofTechnology, under a contract with the National Aeronautics and SpaceAdministration. This work used the Extreme Science and Engineering Discovery Environment (XSEDE; Towns et al., 2014), which is supported by National Science Foundation Grant ACI-1548562. Specifically, this work utilized Stampede and Stampede2 at the Texas Advanced Computing Center (TACC) obtained through XSEDE allocation TG-DPP150005. Figures were created using the Generic Mapping Tools (GMT; Wessel & Smith, 1998). The Voigt average shear wave speed structure of ANT-20 can be obtained through the Incorporated Research Institutions for Seismology (IRIS) Earth Model Collaboration (http://ds.iris.edu/ds/products/emc/). The facilities of IRIS Data Services, and specifically the IRIS Data Management Center, were used for access to waveforms, related metadata, and/or derived products used in this study. IRIS Data Services are funded through the Seismological Facilities for the Advancement of Geoscience and EarthScope (SAGE) Proposal of the National Science Foundation under Cooperative Agreement EAR-1261681. Finally, We thank Martha Savage, Ved Lekic, Andreas Fichtner, and an anonymous reviewer for their critiques on this manuscript.

References

Adhikari, S., Ivins, E. R., Larour, E., Seroussi, H., Morlighem, M., & Nowicki, S. (2014). Future Antarctic bed topography and its implications for ice sheet dynamics. *Solid Earth*, *5*(1), 569–584. https://doi.org/10.5194/se-5-569-2014

Aitken, A. R. A., Young, D. A., Ferraccioli, F., Betts, P. G., Greenbaum, J. S., Richter, T. G., et al. (2014). The subglacial geology of Wilkes Land, East Antarctica. *Geophysical Research Letters*, *41*(7), 2390–2400. https://doi.org/10.1002/2014GL059405

Allibone, A., & Wysoczanski, R. (2002). Initiation of magmatism during the Cambrian–Ordovician Ross orogeny in southern Victoria Land, Antarctica. *Geological Society of America Bulletin*, *114*(8), 1007–1018. https://doi.org/10.1130/0016-7606(2002)114<1007:IOMDTC>2.0.CO;2

Amante, C., & Eakins, B. W. (2009). *ETOPO1 Arc-Minute Global Relief Model: Procedures, Data Sources and Analysis.*

An, M., Wiens, D. A., Zhao, Y., Feng, M., Nyblade, A., Kanao, M., et al. (2015b). Temperature, lithosphere-asthenosphere boundary, and heat flux beneath the Antarctic plate inferred from seismic velocities. *Journal of Geophysical Research: Solid Earth*, *120*, 8720–8742. https://doi.org/10.1002/2015JB011917

An, M., Wiens, D. A., Zhao, Y., Feng, M., Nyblade, A. A., Kanao, M., et al. (2015a). S-velocity model and inferred Moho topography beneath the Antarctic plate from Rayleigh waves. *Journal of Geophysical Research: Solid Earth*, *120*, 359–383. https://doi.org/10.1002/2014JB011332

Babuska, V., & Cara, M. (1991). *Seismic Anisotropy in the Earth*, (Vol. 10). Springer Science & Business Media. https://doi.org/10.1007/978-94-011-3600-6

Bamberger, A., Chavent, G., Hemon, C., & Lailly, P. (1982). Inversion of normal incidence seismograms. *Geophysics*, *47*(5), 757–770. https://doi.org/10.1190/1.1441345

Barletta, V. R., Bevis, M., Smith, B. E., Wilson, T., Brown, A., Bordoni, A., et al. (2018). Observed rapid bedrock uplift in Amundsen Sea embayment promotes ice-sheet stability. *Science*, *360*(6395), 1335–1339. https://doi.org/10.1126/science.aao1447

Bayer, B., Geissler, W. H., Eckstaller, A., & Jokat, W. (2009). Seismic imaging of the crust beneath Dronning Maud land, East Antarctica. *Geophysical Journal International*, *178*(2), 860–876. https://doi.org/10.1111/j.1365-246X.2009.04196.x

Behrendt, J. C. (1999). Crustal and lithospheric structure of the West Antarctic rift system from geophysical investigations—A review. *Global and Planetary Change*, *23*(1-4), 25–44. https://doi.org/10.1016/S0921-8181(99)00049-1

Behrendt, J. C., LeMasurier, W. E., Cooper, A. K., Tessensohn, F., Trehu, A., & Damaske, D. (1991). Geophysical studies of the West Antarctic rift system. *Tectonics*, *10*(6), 1257–1273. https://doi.org/10.1029/91TC00868

Behrendt, J. C., Saltus, R., Damaske, D., McCafferty, A., Finn, C. A., Blankenship, D., & Bell, R. E. (1996). Patterns of late Cenozoic volcanic and tectonic activity in the West Antarctic rift system revealed by aeromagnetic surveys. *Tectonics*, *15*(3), 660–676. https://doi.org/10.1029/95TC03500

Berg, J. H., D. Weis, W.C. McIntosh, and B.I. Cameron (1997), Age and origin of HIMU Volcanism in the Ballany Islands: Melting of plume-delivered deep mantle or shallow asthenospheric mantle?, V. M. Goldschmidt Conference abstracts, number 2362.

Bingham, R. G., Ferraccioli, F., King, E. C., Larter, R. D., Pritchard, H. D., Smith, A. M., & Vaughan, D. G. (2012). Inland thinning of West Antarctic ice sheet steered along subglacial rifts. *Nature*, *487*(7408), 468–471. https://doi.org/10.1038/nature11292

Bird, P. (2003). An updated digital model of plate boundaries. *Geochemistry, Geophysics, Geosystems*, *4*(3), 1027. https://doi.org/10.1029/2001GC000252

Boger, S. D. (2011). Antarctica—Before and after Gondwana. *Gondwana Research*, *19*(2), 335–371. https://doi.org/10.1016/j.gr.2010.09.003

Bozdağ, E., Peter, D., Lefebvre, M., Komatitsch, D., Tromp, J., Hill, J., et al. (2016). Global adjoint tomography: First-generation model. *Geophysical Journal International*, *207*(3), 1739–1766. https://doi.org/10.1093/gji/ggw356

Brenn, G. R., Hansen, S. E., & Park, Y. (2017). Variable thermal loading and flexural uplift along the Transantarctic Mountains, Antarctica. *Geology*, *45*(5), 463–466. https://doi.org/10.1130/G38784.1

Burton-Johnson, A., Black, M., Fretwell, P., & Kaluza-Gilbert, J. (2016). An automated methodology for differentiating rock from snow, clouds and sea in Antarctica from Landsat 8 imagery: A new rock outcrop map and area estimation for the entire Antarctic continent. *The Cryosphere*, *10*(4), 1665–1677. https://doi.org/10.5194/tc-10-1665-2016

Camp, V. E., & Hanan, B. B. (2008). A plume-triggered delamination origin for the Columbia River basalt group. *Geosphere*, *4*(3), 480–495. https://doi.org/10.1130/GES00175.1

Cande, S. C., & Stock, J. M. (2004). *Cenozoic Reconstructions of the Australia-New Zealand-South Pacific Sector of Antarctica*, DOI: https://doi.org/10.1029/151GM02.

Cande, S. C., Stock, J. M., Müller, R. D., & Ishihara, T. (2000). Cenozoic motion between east and West Antarctica. *Nature*, *404*(6774), 145–150. https://doi.org/10.1038/35004501

Canuto, C., Hussaini, M. Y., Quarteroni, A., & Zang, T. A. (1988). *Spectral Methods in Fluid Dynamics*. New York: Springer-Verlag. https://doi.org/10.1007/978-3-642-84108-8

Cawood, P. A. (2005). Terra Australis Orogen: Rodinia breakup and development of the Pacific and Iapetus margins of Gondwana during the Neoproterozoic and Paleozoic. *Earth-Science Reviews*, *69*(3-4), 249–279. https://doi.org/10.1016/j.earscirev.2004.09.001

Chang, S. J., Ferreira, A. M., Ritsema, J., van Heijst, H. J., & Woodhouse, J. H. (2015). Joint inversion for global isotropic and radially anisotropic mantle structure including crustal thickness perturbations. *Journal of Geophysical Research: Solid Earth*, *120*, 4278–4300. https://doi.org/10.1002/2014JB011824

Chaput, J., Aster, R. C., Huerta, A., Sun, X., Lloyd, A., Wiens, D., et al. (2014). The crustal thickness of West Antarctica. *Journal of Geophysical Research: Solid Earth*, *119*, 378–395. https://doi.org/10.1002/2013JB010642

Chaput, J., Aster, R. C., McGrath, D., Baker, M., Anthony, R. E., Gerstoft, P., et al. (2018). Near-surface environmentally forced changes in the Ross ice shelf observed with ambient seismic noise. *Geophysical Research Letters*, *45*(20), 11–187.

Chen, M., Niu, F., Liu, Q., Tromp, J., & Zheng, X. (2015). Multiparameter adjoint tomography of the crust and upper mantle beneath East Asia: 1. Model construction and comparisons. *Journal of Geophysical Research: Solid Earth*, *120*, 1762–1786. https://doi.org/10.1002/2014JB011638

Cogley, J. G. (1984). Deglacial hypsometry of Antarctica. *Earth and Planetary Science Letters*, *67*(3), 284–296. https://doi.org/10.1016/0012-821X(84)90168-7

Cooper, A. F., Adam, L. J., Coulter, R. F., Eby, G. N., & McIntosh, W. C. (2007). Geology, geochronology and geochemistry of a basanitic volcano, White Island, Ross Sea, Antarctica. *Journal of Volcanology and Geothermal Research*, *165*(3-4), 189–216. https://doi.org/10.1016/j.jvolgeores.2007.06.003

Corr, H. F., & Vaughan, D. G. (2008). A recent volcanic eruption beneath the West Antarctic ice sheet. *Nature Geoscience*, *1*(2), 122–125. https://doi.org/10.1038/ngeo106

Dalziel, I. W. (1991). Pacific margins of Laurentia and East Antarctica-Australia as a conjugate rift pair: Evidence and implications for an Eocambrian supercontinent. *Geology*, *19*(6), 598–601. https://doi.org/10.1130/0091-7613(1991)019<0598:PMOLAE>2.3.CO;2

Dalziel, I. W. (1992). Antarctica: A tale of two supercontinents? *Annual Review of Earth and Planetary Sciences*, *20*(1), 501–526. https://doi.org/10.1146/annurev.ea.20.050192.002441

Dalziel, I. W., & Elliot, D. H. (1982). West Antarctica: Problem child of Gondwanaland. *Tectonics*, *1*(1), 3–19. https://doi.org/10.1029/TC001i001p00003

Dalziel, I. W., Lawver, L. A., Norton, I. O., & Gahagan, L. M. (2013). The scotia arc: Genesis, evolution, global significance. *Annual Review of Earth and Planetary Sciences*, *41*(1), 767–793. https://doi.org/10.1146/annurev-earth-050212-124155

Danesi, S., & Morelli, A. (2001). Structure of the upper mantle under the Antarctic plate from surface wave tomography. *Geophysical Research Letters*, *28*(23), 4395–4398. https://doi.org/10.1029/2001GL013431

Donnellan, A., & Luyendyk, B. P. (2004). GPS evidence for a coherent Antarctic plate and for postglacial rebound in Marie Byrd Land. *Global and Planetary Change*, *42*(1-4), 305–311. https://doi.org/10.1016/j.gloplacha.2004.02.006

Durek, J. J., & Ekström, G. (1996). A radial model of anelasticity consistent with long-period surface-wave attenuation. *Bulletin of the Seismological Society of America*, *86*(1A), 144–158.

Eagles, G. (2004). Tectonic evolution of the Antarctic–Phoenix plate system since 15 Ma. *Earth and Planetary Science Letters*, *217*(1-2), 97, Q07002–109. https://doi.org/10.1016/S0012-821X(03)00584-3

Eagles, G., Gohl, K., & Larter, R. D. (2004). High-resolution animated tectonic reconstruction of the South Pacific and West Antarctic margin. *Geochemistry, Geophysics, Geosystems*, *5*, Q07004. https://doi.org/10.1029/2003GC000657

Eagles, G., Larter, R. D., Gohl, K., & Vaughan, A. P. (2009). West Antarctic rift system in the Antarctic peninsula. *Geophysical Research Letters*, *36*, L21305. https://doi.org/10.1029/2009GL040721

Ekström, G., Nettles, M., & Dziewoński, A. M. (2012). The global CMT project 2004–2010: Centroid-moment tensors for 13,017 earthquakes. *Physics of the Earth and Planetary Interiors*, *200*, 1–9. https://doi.org/10.1016/j.pepi.2012.04.002

Emry, E. L., Nyblade, A. A., Julià, J., Anandakrishnan, S., Aster, R. C., Wiens, D. A., et al. (2015). The mantle transition zone beneath West Antarctica: Seismic evidence for hydration and thermal upwellings. *Geochemistry, Geophysics, Geosystems*, *16*, 40–58. https://doi.org/10.1002/2014GC005588

Faccioli, E., Maggio, F., Paolucci, R., & Quarteroni, A. (1997). 2D and 3D elastic wave propagation by a pseudo-spectral domain decomposition method. *Journal of Seismology*, *1*(3), 237–251. https://doi.org/10.1023/A:1009758820546

Faccioli, E., Maggio, F., Quarteroni, A., & Taghan, A. (1996). Spectral-domain decomposition methods for the solution of acoustic and elastic wave equations. *Geophysics*, *61*(4), 1160–1174. https://doi.org/10.1190/1.1444036

Ferraccioli, F., Finn, C. A., Jordan, T. A., Bell, R. E., Anderson, L. M., & Damaske, D. (2011). East Antarctic rifting triggers uplift of the Gamburtsev Mountains. *Nature*, *479*(7373), 388–392. https://doi.org/10.1038/nature10566

Fichtner, A., Kennett, B. L., Igel, H., & Bunge, H. P. (2009). Full seismic waveform tomography for upper-mantle structure in the Australasian region using adjoint methods. *Geophysical Journal International*, *179*(3), 1703–1725. https://doi.org/10.1111/j.1365-246X.2009.04368.x

Fichtner, A., & Leeuwen, T. V. (2015). Resolution analysis by random probing. *Journal of Geophysical Research: Solid Earth*, *120*, 5549–5573. https://doi.org/10.1002/2015JB012106

Fichtner, A., & Trampert, J. (2011). Resolution analysis in full waveform inversion. *Geophysical Journal International*, *187*(3), 1604–1624. https://doi.org/10.1111/j.1365-246X.2011.05218.x

Fielding, C. R., Whittaker, J., Henrys, S. A., Wilson, T. J., & Naish, T. R. (2008). Seismic facies and stratigraphy of the Cenozoic succession in McMurdo Sound, Antarctica: Implications for tectonic, climatic and glacial history. *Palaeogeography, Palaeoclimatology, Palaeoecology*, *260*(1-2), 8–29. https://doi.org/10.1016/j.palaeo.2007.08.016

Fitzgerald, P. A. U. L. (2002). Tectonics and landscape evolution of the Antarctic plate since the breakup of Gondwana, with an emphasis on the West Antarctic Rift System and the Transantarctic Mountains. *Royal Society of New Zealand Bulletin*, *35*, 453–469.

Fitzsimons, I. C. W. (2000a). Grenville-age basement provinces in East Antarctica: Evidence for three separate collisional orogens. *Geology*, *28*(10), 879–882. https://doi.org/10.1130/0091-7613(2000)28<879:GBPIEA>2.0.CO;2

Fitzsimons, I. C. W. (2000b). A review of tectonic events in the East Antarctic shield and their implications for Gondwana and earlier supercontinents. *Journal of African Earth Sciences*, *31*(1), 3–23. https://doi.org/10.1016/S0899-5362(00)00069-5

Fitzsimons, I. C. W. (2003). Proterozoic basement provinces of southern and southwestern Australia, and their correlation with Antarctica. *Geological Society, London, Special Publications*, *206*(1), 93–130. https://doi.org/10.1144/GSL.SP.2003.206.01.07

Fletcher, R., & Reeves, C. M. (1964). Function minimization by conjugate gradients. *The Computer Journal*, *7*(2), 149–154. https://doi.org/10.1093/comjnl/7.2.149

French, S. W., & Romanowicz, B. A. (2014). Whole-mantle radially anisotropic shear velocity structure from spectral-element waveform tomography. *Geophysical Journal International*, *199*(3), 1303–1327.

French, S., Lekic, V., & Romanowicz, B. (2013). Waveform tomography reveals channeled flow at the base of the oceanic asthenosphere. *Science*, *342*(6155), 227–230. https://doi.org/10.1126/science.1241514

Fretwell, P., Pritchard, H. D., Vaughan, D. G., Bamber, J. L., Barrand, N. E., Bell, R., et al. (2013). Bedmap2: Improved ice bed, surface and thickness datasets for Antarctica. *The Cryosphere*, *7*(1), 375–393. https://doi.org/10.5194/tc-7-375-2013

Gomez, N., Latychev, K., & Pollard, D. (2018). A coupled ice sheet–sea level model incorporating 3D earth structure: Variations in Antarctica during the last deglacial retreat. *Journal of Climate*, *31*(10), 4041–4054. https://doi.org/10.1175/JCLI-D-17-0352.1

Gomez, N., Pollard, D., & Holland, D. (2015). Sea-level feedback lowers projections of future Antarctic ice-sheet mass loss. *Nature Communications*, *6*(1), 8798. https://doi.org/10.1038/ncomms9798

Goodge, J. W., Fanning, C. M., & Bennett, V. C. (2001). U–Pb evidence of ~1.7 Ga crustal tectonism during the nimrod orogeny in the Transantarctic Mountains, Antarctica: Implications for Proterozoic plate reconstructions. *Precambrian Research*, *112*(3-4), 261–288. https://doi.org/10.1016/S0301-9268(01)00193-0

Goodge, J. W., Fanning, C. M., Fisher, C. M., & Vervoort, J. D. (2017). Proterozoic crustal evolution of central East Antarctica: Age and isotopic evidence from glacial igneous clasts, and links with Australia and Laurentia. *Precambrian Research*, *299*, 151–176. https://doi.org/10.1016/j.precamres.2017.07.026

Goodge, J. W., & Finn, C. A. (2010). Glimpses of East Antarctica: Aeromagnetic and satellite magnetic view from the central Transantarctic Mountains of East Antarctica. *Journal of Geophysical Research - Solid Earth*, *115*. https://doi.org/10.1029/2009JB006890

Grand, S. P., & Helmberger, D. V. (1984). Upper mantle shear structure of North America. *Geophysical Journal International*, *76*(2), 399–438. https://doi.org/10.1111/j.1365-246X.1984.tb05053.x

Granot, R., Cande, S. C., Stock, J. M., & Damaske, D. (2013). Revised Eocene-Oligocene kinematics for the West Antarctic rift system. *Geophysical Research Letters*, *40*, 279–284. https://doi.org/10.1029/2012GL054181

Granot, R., Cande, S. C., Stock, J. M., Davey, F. J., & Clayton, R. W. (2010). Postspreading rifting in the Adare Basin, Antarctica: Regional tectonic consequences. *Geochemistry, Geophysics, Geosystems*, *11*, Q08005. https://doi.org/10.1029/2010GC003105

Granot, R., & Dyment, J. (2018). Late Cenozoic unification of east and West Antarctica. *Nature Communications*, *9*, 3189. https://doi.org/10.1038/s41467-018-05270-w

Graw, J. H., Adams, A. N., Hansen, S. E., Wiens, D. A., Hackworth, L., & Park, Y. (2016). Upper mantle shear wave velocity structure beneath northern Victoria land, Antarctica: Volcanism and uplift in the northern Transantarctic Mountains. *Earth and Planetary Science Letters*, *449*, 48–60. https://doi.org/10.1016/j.epsl.2016.05.026

Groh, A., Ewert, H., Scheinert, M., Fritsche, M., Rülke, A., Richter, A., et al. (2012). An investigation of glacial isostatic adjustment over the Amundsen Sea sector, West Antarctica. *Global and Planetary Change*, *98-99*, 45–53. https://doi.org/10.1016/j.gloplacha.2012.08.001

Groome, W. G., & Thorkelson, D. J. (2009). The three-dimensional thermo-mechanical signature of ridge subduction and slab window migration. *Tectonophysics*, *464*(1-4), 70–83. https://doi.org/10.1016/j.tecto.2008.07.003

Grunow, A. M., Dalziel, I. W. D., & Kent, D. V. (1987). *Ellsworth-Whitmore Mountains Crustal Block, Western Antarctica: New Paleomagnetic Results and their Tectonic Significance*.

Grunow, A. M., Kent, D. V., & Dalziel, I. W. D. (1991). New paleomagnetic data from Thurston Island: Implications for the tectonics of West Antarctica and Weddell Sea opening. *Journal of Geophysical Research - Solid Earth*, *96*, 17935–17954. https://doi.org/10.1029/91JB01507

Hansen, S. E., Graw, J. H., Kenyon, L. M., Nyblade, A. A., Wiens, D. A., Aster, R. C., et al. (2014). Imaging the Antarctic mantle using adaptively parameterized P-wave tomography: Evidence for heterogeneous structure beneath West Antarctica. *Earth and Planetary Science Letters*, *408*, 66–78. https://doi.org/10.1016/j.epsl.2014.09.043

Hansen, S. E., Julia, J., Nyblade, A. A., Pyle, M. L., Wiens, D. A., & Anandakrishnan, S. (2009). Using S wave receiver functions to estimate crustal structure beneath ice sheets: An application to the Transantarctic Mountains and East Antarctic craton. *Geochemistry, Geophysics, Geosystems*, *10*, Q08014. https://doi.org/10.1029/2009GC002576

Hansen, S. E., Nyblade, A. A., Heeszel, D. S., Wiens, D. A., Shore, P., & Kanao, M. (2010). Crustal structure of the Gamburtsev Mountains, East Antarctica, from S-wave receiver functions and Rayleigh wave phase velocities. *Earth and Planetary Science Letters*, *300*(3-4), 395–401. https://doi.org/10.1016/j.epsl.2010.10.022

Hansen, S. E., Reusch, A. M., Parker, T., Bloomquist, D. K., Carpenter, P., Graw, J. H., & Brenn, G. R. (2015). The Transantarctic Mountains northern network (TAMNNET): Deployment and performance of a seismic array in Antarctica. *Seismological Research Letters*, *86*(6), 1636–1644. https://doi.org/10.1785/0220150117

Harry, D. L., Anoka, J. L., & Jha, S. (2018). Geodynamic models of the West Antarctic rift system: Implications for the mantle thermal state. *Geosphere*, *14*(6), 2407–2429. https://doi.org/10.1130/GES01594.1

Hay, C. C., Lau, H. C., Gomez, N., Austermann, J., Powell, E., Mitrovica, J. X., et al. (2017). Sea level fingerprints in a region of complex earth structure: The case of WAIS. *Journal of Climate*, *30*(6), 1881–1892. https://doi.org/10.1175/JCLI-D-16-0388.1

Heeszel, D. S., Wiens, D. A., Anandakrishnan, S., Aster, R. C., Dalziel, I. W., Huerta, A. D., et al. (2016). Upper mantle structure of central and West Antarctica from array analysis of Rayleigh wave phase velocities. *Journal of Geophysical Research: Solid Earth*, *121*, 1758–1775. https://doi.org/10.1002/2015JB012616

Heeszel, D. S., Wiens, D. A., Nyblade, A. A., Hansen, S. E., Kanao, M., An, M., & Zhao, Y. (2013). Rayleigh wave constraints on the structure and tectonic history of the Gamburtsev Subglacial Mountains, East Antarctica. *Journal of Geophysical Research: Solid Earth*, *118*, 2138–2153. https://doi.org/10.1002/jgrb.50171

Henrys, S. A., Wilson, T. J., Fielding, C. R., Hall, J., & Naish, T. R. (2008). *Tectonic History of mid-Miocene to Present Southern Victoria Land Basin, Inferred from Seismic Stratigraphy in McMurdo Sound, Antarctica*.

Hjörleifsdóttir, V., & Ekström, G. (2010). Effects of three-dimensional earth structure on CMT earthquake parameters. *Physics of the Earth and Planetary Interiors*, *179*(3-4), 178–190. https://doi.org/10.1016/j.pepi.2009.11.003

Hoffman, P. F. (1991). Did the breakout of Laurentia turn Gondwanaland inside-out? *Science*, *252*(5011), 1409–1412. https://doi.org/10.1126/science.252.5011.1409

Ivins, E. R., & Sammis, C. G. (1995). On lateral viscosity contrast in the mantle and the rheology of low-frequency geodynamics. *Geophysical Journal International*, *123*(2), 305–322. https://doi.org/10.1111/j.1365-246X.1995.tb06856.x

Jacobs, J., Bingen, B., Thomas, R. J., Bauer, W., Wingate, M. T., & Feitio, P. (2008). Early Palaeozoic orogenic collapse and voluminous late-tectonic magmatism in Dronning Maud land and Mozambique: Insights into the partially delaminated orogenic root of the east African–Antarctic Orogen? *Geological Society, London, Special Publications*, *308*(1), 69–90. https://doi.org/10.1144/SP308.3

Jordan, T. A., Ferraccioli, F., Ross, N., Corr, H. F., Leat, P. T., Bingham, R. G., et al. (2013). Inland extent of the Weddell Sea Rift imaged by new aerogeophysical data. *Tectonophysics*, *585*, 137–160.

Jordan, T. A., Ferraccioli, F., Vaughan, D. G., Holt, J. W., Corr, H., Blankenship, D. D., & Diehl, T. M. (2010). Aerogravity evidence for major crustal thinning under the Pine Island glacier region (West Antarctica). *Bulletin of the Geological Society of America*, *122*(5-6), 714–726. https://doi.org/10.1130/B26417.1

Jordan, T. H. (1975). The continental tectosphere. *Reviews of Geophysics*, *13*(3), 1–12. https://doi.org/10.1029/RG013i003p00001

Kaufmann, G., Wu, P., & Ivins, E. R. (2005). Lateral viscosity variations beneath Antarctica and their implications on regional rebound motions and seismotectonics. *Journal of Geodynamics*, *39*(2), 165–181. https://doi.org/10.1016/j.jog.2004.08.009

Kelly, N. M., & Harley, S. L. (2005). An integrated microtextural and chemical approach to zircon geochronology: Refining the Archaean history of the Napier complex, East Antarctica. *Contributions to Mineralogy and Petrology*, *149*(1), 57–84. https://doi.org/10.1007/s00410-004-0635-6

Kipf, A., Hauff, F., Werner, R., Gohl, K., van den Bogaard, P., Hoernle, K., et al. (2014). Seamounts off the West Antarctic margin: A case for non-hotspot driven intraplate volcanism. *Gondwana Research*, *25*(4), 1660–1679. https://doi.org/10.1016/j.gr.2013.06.013

Komatitsch, D., & Tromp, J. (1999). Introduction to the spectral element method for three-dimensional seismic wave propagation. *Geophysical Journal International*, *139*(3), 806–822. https://doi.org/10.1046/j.1365-246x.1999.00967.x

Komatitsch, D., & Tromp, J. (2002a). Spectral-element simulations of global seismic wave propagation—I. Validation. *Geophysical Journal International*, *149*(2), 390–412. https://doi.org/10.1046/j.1365-246X.2002.01653.x

Komatitsch, D., & Tromp, J. (2002b). Spectral-element simulations of global seismic wave propagation—II. Three-dimensional models, oceans, rotation and self-gravitation. *Geophysical Journal International*, *150*(1), 303–318. https://doi.org/10.1046/j.1365-246X.2002.01716.x

Komatitsch, D., & Vilotte, J. P. (1998). The spectral element method: An efficient tool to simulate the seismic response of 2D and 3D geological structures. *Bulletin of the Seismological Society of America*, *88*(2), 368–392.

Komatitsch, D., Xie, Z., Bozdağ, E., Sales de Andrade, E., Peter, D., Liu, Q., & Tromp, J. (2016). Anelastic sensitivity kernels with parsimonious storage for adjoint tomography and full waveform inversion. *Geophysical Journal International*, *206*(3), 1467–1478. https://doi.org/10.1093/gji/ggw224

Konrad, H., Sasgen, I., Pollard, D., & Klemann, V. (2015). Potential of the solid-earth response for limiting long-term West Antarctic ice sheet retreat in a warming climate. *Earth and Planetary Science Letters*, *432*, 254–264. https://doi.org/10.1016/j.epsl.2015.10.008

Kustowski, B., Ekström, G., & Dziewoński, A. M. (2008). Anisotropic shear-wave velocity structure of the Earth's mantle: A global model. *Journal of Geophysical Research - Solid Earth*, *113*. https://doi.org/10.1029/2007JB005169

Kyle, P. R. (1990). A. McMurdo volcanic group western Ross embayment. *Volcanoes of the Antarctic plate and southern Oceans*, *48*, 18–145. https://doi.org/10.1029/AR048p0018

Kyle, P. R., Moore, J. A., & Thirlwall, M. F. (1992). Petrologic evolution of anorthoclase phonolite lavas at mount Erebus, Ross Island, Antarctica. *Journal of Petrology*, *33*(4), 849–875. https://doi.org/10.1093/petrology/33.4.849

Larter, R. D., Rebesco, M., Vanneste, L. E., Gamboa, L. A. P., & Barker, P. F. (1997). Cenozoic tectonic, sedimentary and glacial history of the continental shelf west of Graham Land, Antarctic peninsula. In *Geology and seismic stratigraphy of the Antarctic margin*, (Vol. 2, pp. 1–27).

Laske, G., & Masters, G. (1998). Surface-wave polarization data and global anisotropic structure. *Geophysical Journal International*, *132*(3), 508–520. https://doi.org/10.1046/j.1365-246X.1998.00450.x

Laske, G., Masters, G., Ma, Z., & Pasyanos, M. (2013, April). Update on CRUST1. 0—A 1-degree global model of Earth's crust. In *Geophys. Res. Abstr*, (Vol. 15, p. 2658). Vienna, Austria: EGU General Assembly.

Lawrence, J. F., Wiens, D. A., Nyblade, A. A., Anandakrishan, S., Shore, P. J., & Voigt, D. (2006a). Upper mantle thermal variations beneath the Transantarctic Mountains inferred from teleseismic S-wave attenuation. *Geophysical Research Letters*, *33*, L03303. https://doi.org/10.1029/2005GL024516

Lawrence, J. F., Wiens, D. A., Nyblade, A. A., Anandakrishnan, S., Shore, P. J., & Voigt, D. (2006b). Rayleigh wave phase velocity analysis of the Ross Sea, Transantarctic Mountains, and East Antarctica from a temporary seismograph array. *Journal of Geophysical Research - Solid Earth*, *111*. https://doi.org/10.1029/2005JB003812

Lebedev, S., Boonen, J., & Trampert, J. (2009). Seismic structure of Precambrian lithosphere: New constraints from broad-band surface-wave dispersion. *Lithos*, *109*(1-2), 96–111. https://doi.org/10.1016/j.lithos.2008.06.010

Lekic, V., Cottaar, S., Dziewonski, A., & Romanowicz, B. (2012). Cluster analysis of global lower mantle tomography: A new class of structure and implications for chemical heterogeneity. *Earth and Planetary Science Letters*, *357-358*, 68–77. https://doi.org/10.1016/j.epsl.2012.09.014

LeMasurier, W. E. (1990). Late Cenozoic volcanism on the Antarctic plate: An overview. *Volcanoes of the Antarctic plate and southern oceans*, *48*, 1–17. https://doi.org/10.1029/AR048p0001

LeMasurier, W. E. (2008). Neogene extension and basin deepening in the West Antarctic rift inferred from comparisons with the east African rift and other analogs. *Geology*, *36*(3), 247–250. https://doi.org/10.1130/G24363A.1

LeMasurier, W. E., & Landis, C. A. (1996). Mantle-plume activity recorded by low-relief erosion surfaces in West Antarctica and New Zealand. *Geological Society of America Bulletin*, *108*(11), 1450–1466. https://doi.org/10.1130/0016-7606(1996)108<1450:MPARBL>2.3.CO;2

LeMasurier, W. E., & Rex, D. C. (1989). Evolution of linear volcanic ranges in Marie Byrd Land, West Antarctica. *Journal of Geophysical Research: Solid Earth*, *94*(B6), 7223–7236. https://doi.org/10.1029/JB094iB06p07223

Licht, K. J., Groth, T., Townsend, J. P., Hennessy, A. J., Hemming, S. R., Flood, T. P., & Studinger, M. (2018). Evidence for extending anomalous Miocene volcanism at the edge of the East Antarctic craton. *Geophysical Research Letters*, *45*(7), 3009–3016. https://doi.org/10.1002/2018GL077237

Liu, Q., Polet, J., Komatitsch, D., & Tromp, J. (2004). Spectral-element moment tensor inversions for earthquakes in southern California. *Bulletin of the Seismological Society of America*, *94*(5), 1748–1761. https://doi.org/10.1785/012004038

Lloyd, A. J., Nyblade, A. A., Wiens, D. A., Hansen, S. E., Kanao, M., Shore, P. J., & Zhao, D. (2013). Upper mantle seismic structure beneath central East Antarctica from body wave tomography: Implications for the origin of the Gamburtsev Subglacial Mountains. *Geochemistry, Geophysics, Geosystems*, *14*, 902–920. https://doi.org/10.1002/ggge.20098

Lloyd, A. J., Wiens, D. A., Nyblade, A. A., Anandakrishnan, S., Aster, R. C., Huerta, A. D., et al. (2015). A seismic transect across West Antarctica: Evidence for mantle thermal anomalies beneath the Bentley subglacial trench and the Marie Byrd Land dome. *Journal of Geophysical Research: Solid Earth*, *120*, 8439–8460. https://doi.org/10.1002/2015JB012455

Lough, A. C., Wiens, D. A., Barcheck, C. G., Anandakrishnan, S., Aster, R. C., Blankenship, D. D., et al. (2013). Seismic detection of an active subglacial magmatic complex in Marie Byrd Land, Antarctica. *Nature Geoscience*, *6*(12), 1031–1035. https://doi.org/10.1038/ngeo1992

Luo, Y., & Schuster, G. T. (1991). Wave-equation traveltime inversion. *Geophysics*, *56*(5), 645–653. https://doi.org/10.1190/1.1443081

Luo, Y., Tromp, J., Denel, B., & Calandra, H. (2013). 3D coupled acoustic-elastic migration with topography and bathymetry based on spectral-element and adjoint methods. *Geophysics*, *78*(4), S193–S202. https://doi.org/10.1190/geo2012-0462.1

Luyendyk, B., Cisowski, S., Smith, C., Richard, S., & Kimbrough, D. (1996). Paleomagnetic study of the northern ford ranges, western Marie Byrd Land, West Antarctica: Motion between west and East Antarctica. *Tectonics*, *15*(1), 122–141. https://doi.org/10.1029/95TC02524

Luyendyk, B. P. (1995). Hypothesis for cretaceous rifting of East Gondwana caused by subducted slab capture. *Geology*, *23*(4), 373–376. https://doi.org/10.1130/0091-7613(1995)023<0373:HFCROE>2.3.CO;2

Luyendyk, B. P., Wilson, D. S., & Siddoway, C. S. (2003). Eastern margin of the Ross Sea rift in western Marie Byrd Land, Antarctica: Crustal structure and tectonic development. *Geochemistry, Geophysics, Geosystems*, *4*(10), 1090. https://doi.org/10.1029/2002GC000462

Maggi, A., Tape, C., Chen, M., Chao, D., & Tromp, J. (2009). An automated time-window selection algorithm for seismic tomography. *Geophysical Journal International*, *178*(1), 257–281. https://doi.org/10.1111/j.1365-246X.2009.04099.x

Montagner, J. P., & Anderson, D. L. (1989). Petrological constraints on seismic anisotropy. *Physics of the Earth and Planetary Interiors*, *54*(1-2), 82–105. https://doi.org/10.1016/0031-9201(89)90189-1

Moores, E. M. (1991). Southwest US-East Antarctic (SWEAT) connection: A hypothesis. *Geology*, *19*(5), 425–428. https://doi.org/10.1130/0091-7613(1991)019<0425:SUSEAS>2.3.CO;2

Mortimer, N., Dunlap, W. J., Isaac, M. J., Sutherland, R. P., & Faure, K. (2007). Basal Adare volcanics, Robertson Bay, North Victoria Land, Antarctica: Late Miocene intraplate basalts of subaqueous origin (No. 2007-1047-SRP-045). US Geological Survey.

Mukasa, S. B., & Dalziel, I. W. (2000). Marie Byrd Land, West Antarctica: Evolution of Gondwana's Pacific margin constrained by zircon U-Pb geochronology and feldspar common-Pb isotopic compositions. *Geological Society of America Bulletin*, *112*(4), 611–627. https://doi.org/10.1130/0016-7606(2000)112<611:MBLWAE>2.0.CO;2

Müller, R. D., Gohl, K., Cande, S. C., Goncharov, A., & Golynsky, A. V. (2007). Eocene to Miocene geometry of the West Antarctic rift system. *Australian Journal of Earth Sciences*, *54*(8), 1033–1045. https://doi.org/10.1080/08120090701615691

Nield, G. A., Barletta, V. R., Bordoni, A., King, M. A., Whitehouse, P. L., Clarke, P. J., et al. (2014). Rapid bedrock uplift in the Antarctic peninsula explained by viscoelastic response to recent ice unloading. *Earth and Planetary Science Letters*, *397*, 32–41. https://doi.org/10.1016/j.epsl.2014.04.019

O'Donnell, J. P., & Nyblade, A. A. (2014). Antarctica's hypsometry and crustal thickness: Implications for the origin of anomalous topography in East Antarctica. *Earth and Planetary Science Letters*, *388*, 143–155. https://doi.org/10.1016/j.epsl.2013.11.051

O'Donnell, J. P., Selway, K., Nyblade, A. A., Brazier, R. A., Wiens, D. A., Anandakrishnan, S., et al. (2017). The uppermost mantle seismic velocity and viscosity structure of central West Antarctica. *Earth and Planetary Science Letters*, *472*, 38–49. https://doi.org/10.1016/j.epsl.2017.05.016

O'Donnell, J. P., Stuart, G. W., Brisbourne, A. M., Selway, K., Yang, Y., Nield, G. A., et al. (2019). The uppermost mantle seismic velocity structure of West Antarctica from Rayleigh wave tomography: Insights into tectonic structure and geothermal heat flow. *Earth and Planetary Science Letters*, *522*, 219–233. https://doi.org/10.1016/j.epsl.2019.06.024

Panter, K. S., McIntosh, W. C., & Smellie, J. L. (1994). Volcanic history of mount Sidley, a major alkaline volcano in Marie Byrd Land, Antarctica. *Bulletin of Volcanology*, *56*(5), 361–376. https://doi.org/10.1007/BF00326462

Pattyn, F., Carter, S. P., & Thoma, M. (2016). Advances in modelling subglacial lakes and their interaction with the Antarctic ice sheet. *Philosophical Transactions of the Royal Society A: Mathematical, Physical and Engineering Sciences*, *374*(2059), 20140296. https://doi.org/10.1098/rsta.2014.0296

Phillips, G., & Läufer, A. L. (2009). Brittle deformation relating to the Carboniferous–Cretaceous evolution of theLambert Graben, East Antarctica: A precursor for Cenozoic relief development in an intraplate and glaciated region. *Tectonophysics*, *471*(3-4), 216–224. https://doi.org/10.1016/j.tecto.2009.02.012

Phillips, E. H., Sims, K. W., Blichert-Toft, J., Aster, R. C., Gaetani, G. A., Kyle, P. R., et al. (2018). The nature and evolution of mantle upwelling at Ross Island, Antarctica, with implications for the source of HIMU lavas. *Earth and Planetary Science Letters*, *498*, 38–53. https://doi.org/10.1016/j.epsl.2018.05.049

Pollard, D., DeConto, R. M., & Nyblade, A. A. (2005). Sensitivity of Cenozoic Antarctic ice sheet variations to geothermal heat flux. *Global and Planetary Change*, *49*(1-2), 63–74. https://doi.org/10.1016/j.gloplacha.2005.05.003

Powell, C. M., & Pisarevsky, S. A. (2002). Late Neoproterozoic assembly of East Gondwana. *Geology*, *30*(1), 3–6. https://doi.org/10.1130/0091-7613(2002)030<0003:LNAOEG>2.0.CO;2

Randall, D. E., & Mac Niocaill, C. (2004). Cambrian palaeomagnetic data confirm a Natal embayment location for the Ellsworth—Whitmore Mountains, Antarctica, in Gondwana reconstructions. *Geophysical Journal International*, *157*(1), 105–116. https://doi.org/10.1111/j.1365-246X.2004.02192.x

Reading, A. M. (2006). The seismic structure of Precambrian and early Palaeozoic terranes in the Lambert glacier region, East Antarctica. *Earth and Planetary Science Letters*, *244*(1-2), 44–57. https://doi.org/10.1016/j.epsl.2006.01.031

Reusch, A. M., Nyblade, A. A., Benoit, M. H., Wiens, D. A., Anandakrishnan, S., Voigt, D., & Shore, P. J. (2008). Mantle transition zone thickness beneath Ross Island, the Transantarctic Mountains, and East Antarctica. *Geophysical Research Letters*, *35*, L12301. https://doi.org/10.1029/2008GL033873

Ritsema, J., Deuss, A. A., Van Heijst, H. J., & Woodhouse, J. H. (2011). S40RTS: A degree-40 shear-velocity model for the mantle from new Rayleigh wave dispersion, teleseismic traveltime and normal-mode splitting function measurements. *Geophysical Journal International*, *184*(3), 1223–1236. https://doi.org/10.1111/j.1365-246X.2010.04884.x

Ritzwoller, M. H., Shapiro, N. M., Levshin, A. L., & Leahy, G. M. (2001). Crustal and upper mantle structure beneath Antarctica and surrounding oceans. *Journal of Geophysical Research - Solid Earth*, *106*(B12), 30645–30670. https://doi.org/10.1029/2001JB000179

Rocchi, S., Armienti, P., D'Orazio, M., Tonarini, S., Wijbrans, J. R., & Di Vincenzo, G. (2002). Cenozoic magmatism in the western Ross embayment: Role of mantle plume versus plate dynamics in the development of the West Antarctic rift system. *Journal of Geophysical Research - Solid Earth*, *107*(B9). https://doi.org/10.1029/2001JB000515

Rogers, J. J., Unrug, R., & Sultan, M. (1995). Tectonic assembly of Gondwana. *Journal of Geodynamics*, *19*(1), 1–34. https://doi.org/10.1016/0264-3707(94)00007-7

Ronchi, C., Iacono, R., & Paolucci, P. S. (1996). The "cubed sphere": A new method for the solution of partial differential equations in spherical geometry. *Journal of Computational Physics*, *124*(1), 93–114. https://doi.org/10.1006/jcph.1996.0047

Ruppel, A., Jacobs, J., Eagles, G., Läufer, A., & Jokat, W. (2018). New geophysical data from a key region in East Antarctica: Estimates for the spatial extent of the Tonian Oceanic Arc Super Terrane (TOAST). *Gondwana Research*, *59*,97-107.

Russo, R. M., VanDecar, J. C., Comte, D., Mocanu, V. I., Gallego, A., & Murdie, R. E. (2010). Subduction of the Chile ridge: Upper mantle structure and flow. *GSA Today*, *20*(9), 4–10.

Schaeffer, A. J., & Lebedev, S. (2013). Global shear speed structure of the upper mantle and transition zone. *Geophysical Journal International*, *194*(1), 417–449.

Schaeffer, A. J., & Lebedev, S. (2015). Global heterogeneity of the lithosphere and underlying mantle: A seismological appraisal based on multimode surface-wave dispersion analysis, shear-velocity tomography, and tectonic regionalization. In *The Earth's Heterogeneous Mantle*, (pp. 3–46). Cham: Springer. https://doi.org/10.1007/978-3-319-15627-9_1

Schopf, J. M. (1969). Ellsworth Mountains: Position in West Antarctica due to seafloor spreading. *Science*, *164*(3875), 63–66. https://doi.org/10.1126/science.164.3875.63

Seroussi, H., Ivins, E. R., Wiens, D. A., & Bondzio, J. (2017). Influence of a West Antarctic mantle plume on ice sheet basal conditions. *Journal of Geophysical Research: Solid Earth*, *122*, 7127–7155. https://doi.org/10.1002/2017JB014423

Shapiro, N. M., & Ritzwoller, M. H. (2004). Inferring surface heat flux distributions guided by a global seismic model: Particular application to Antarctica. *Earth and Planetary Science Letters*, *223*(1-2), 213–224. https://doi.org/10.1016/j.epsl.2004.04.011

Shen, W., Wiens, D. A., Anandakrishnan, S., Aster, R. C., Gerstoft, P., Bromirski, P. D., et al. (2018). The crust and upper mantle structure of central and West Antarctica from Bayesian inversion of Rayleigh wave and receiver functions. *Journal of Geophysical Research: Solid Earth*, *123*(9), 7824–7849. https://doi.org/10.1029/2017JB015346

Shen, W., Wiens, D. A., Stern, T., Anandakrishnan, S., Aster, R. C., Dalziel, I., et al. (2018). Seismic evidence for lithospheric foundering beneath the southern Transantarctic Mountains, Antarctica. *Geology*, *46*(1), 71–74. https://doi.org/10.1130/G39555.1

Siddoway, C. S. (2008). Tectonics of the West Antarctic rift system: New light on the history and dynamics of distributed intracontinental extension. In *Antarctica: A Keystone in a Changing World*, (pp. 91–114).

Sieminski, A., Debayle, E., & Lévêque, J. J. (2003). Seismic evidence for deep low-velocity anomalies in the transition zone beneath West Antarctica. *Earth and Planetary Science Letters*, *216*(4), 645–661. https://doi.org/10.1016/S0012-821X(03)00518-1

Sirevaag, H., Jacobs, J., Ksienzyk, A. K., Dunkl, I., & Marschall, H. R. (2018). Extent, thickness and erosion of the Jurassic continental flood basalts of Dronning Maud land, East Antarctica: A low-T thermochronological approach. *Gondwana Research*, *61*, 222–243. https://doi.org/10.1016/j.gr.2018.04.017

Smellie, J. L. (1987). Geochemistry and tectonic setting of alkaline volcanic rocks in the Antarctic peninsula: A review. *Journal of Volcanology and Geothermal Research*, *32*(1-3), 269–285. https://doi.org/10.1016/0377-0273(87)90048-5

Stern, T. A., & ten Brink, U. S. (1989). Flexural uplift of the Transantarctic Mountains. *Journal of GeophysicalResearch: Solid Earth*, *94*(B8), 10315–10330.

Stump, E., Sheridan, M. F., Borg, S. G., & Sutter, J. F. (1980). Early Miocene subglacial basalts, the East Antarctic ice sheet, and uplift of the Transantarctic Mountains. *Science*, *207*(4432), 757–759. https://doi.org/10.1126/science.207.4432.757

Tape, C., Liu, Q., Maggi, A., & Tromp, J. (2009). Adjoint tomography of the southern California crust. *Science*, *325*(5943), 988–992. https://doi.org/10.1126/science.1175298

Tape, C., Liu, Q., Maggi, A., & Tromp, J. (2010). Seismic tomography of the southern California crust based on spectral-element and adjoint methods. *Geophysical Journal International*, *180*(1), 433–462. https://doi.org/10.1111/j.1365-246X.2009.04429.x

Tape, C., Liu, Q., & Tromp, J. (2007). Finite-frequency tomography using adjoint methods—Methodology and examples using membrane surface waves. *Geophysical Journal International*, *168*(3), 1105–1129. https://doi.org/10.1111/j.1365-246X.2006.03191.x

Tarantola, A. (1984). Inversion of seismic reflection data in the acoustic approximation. *Geophysics*, *49*(8), 1259–1266. https://doi.org/10.1190/1.1441754

Tingey, R. J. (1991). The regional geology of Archean and Proterozoic rocks in Antarctica. In *The geology of Antarctica*, (pp. 1–73).

Torsvik, T. H., Gaina, C., & Redfield, T. F. (2008). Antarctica and global paleogeography: from Rodinia, through Gondwanaland and Pangea, to the birth of the Southern Ocean and the opening of gateways. Antarctica: A keystone in a changing world, 125-141.

Towns, J., Cockerill, T., Dahan, M., Foster, I., Gaither, K., Grimshaw, A., et al. (2014). XSEDE: Accelerating scientific discovery. *Computing in Science & Engineering*, *16*(5), 62–74. https://doi.org/10.1109/MCSE.2014.80

Trey, H., Cooper, A. K., Pellis, G., & Della Vedova, B., Cochrane, G., Brancolini, G., & Makris, J. (1999). Transect across the West Antarctic rift system in the Ross Sea, Antarctica. *Tectonophysics*, *301*(1-2), 61–74. https://doi.org/10.1016/S0040-1951(98)00155-3

Tromp, J., Komatitsch, D., Hjörleifsdóttir, V., Liu, Q., Zhu, H., Peter, D., et al. (2010). Near real-time simulations of global CMT earthquakes. *Geophysical Journal International*, *183*(1), 381–389. https://doi.org/10.1111/j.1365-246X.2010.04734.x

Tromp, J., Tape, C., & Liu, Q. (2005). Seismic tomography, adjoint methods, time reversal and banana-doughnut kernels. *Geophysical Journal International*, *160*(1), 195–216. https://doi.org/10.1111/j.1365-246X.2004.02453.x

van der Wal, W., Whitehouse, P. L., & Schrama, E. J. (2015). Effect of GIA models with 3D composite mantle viscosity on GRACE mass balance estimates for Antarctica. *Earth and Planetary Science Letters*, *414*, 134–143. https://doi.org/10.1016/j.epsl.2015.01.001

Veevers, J. J., & Saeed, A. (2011). Age and composition of Antarctic bedrock reflected by detrital zircons, erratics, and recycled microfossils in the Prydz Bay–Wilkes Land–Ross Sea–Marie Byrd Land sector (70–240 E). *Gondwana Research*, *20*(4), 710–738. https://doi.org/10.1016/j.gr.2011.03.007

Wannamaker, P., Hill, G., Stodt, J., Maris, V., Ogawa, Y., Selway, K., et al. (2017). Uplift of the central transantarctic mountains. *Nature Communications*, *8*(1), 1588. https://doi.org/10.1038/s41467-017-01577-2

Watson, T., Nyblade, A., Wiens, D. A., Anandakrishnan, S., Benoit, M., Shore, P. J., et al. (2006). P and S velocity structure of the upper mantle beneath the Transantarctic Mountains, East Antarctic craton, and Ross Sea from travel time tomography. *Geochemistry, Geophysics, Geosystems*, *7*, Q07005. https://doi.org/10.1029/2005GC001238

Weaver, S. D., Storey, B. C., Pankhurst, R. J., Mukasa, S. B., DiVenere, V. J., & Bradshaw, J. D. (1994). Antarctica-New Zealand rifting and Marie Byrd Land lithospheric magmatism linked to ridge subduction and mantle plume activity. *Geology*, *22*(9), 811–814. https://doi.org/10.1130/0091-7613(1994)022<0811:ANZRAM>2.3.CO;2

Wessel, P., & Smith, W. H. (1998). New, improved version of generic mapping tools released. *Eos, Transactions American Geophysical Union*, *79*(47), 579–579. https://doi.org/10.1029/98EO00426

White-Gaynor, A. L., Nyblade, A. A., Aster, R. C., Wiens, D. A., Bromirski, P. D., Gerstoft, P., et al. (2019). Heterogeneous upper mantle structure beneath the Ross Sea embayment and Marie Byrd Land, West Antarctica, revealed by P-wave tomography. *Earth and Planetary Science Letters*, *513*, 40–50. https://doi.org/10.1016/j.epsl.2019.02.013

Wilch, T. I., McIntosh, W. C., & Dunbar, N. W. (1999). Late Quaternary volcanic activity in Marie Byrd Land: Potential $^{40}Ar/^{39}Ar$-dated time horizons in West Antarctic ice and marine cores. *Geological Society of America Bulletin*, *111*(10), 1563–1580. https://doi.org/10.1130/0016-7606(1999)111<1563:LQVAIM>2.3.CO;2

Wilson, D. S., & Luyendyk, B. P. (2009). West Antarctic paleotopography estimated at the Eocene-Oligocene climate transition. *Geophysical Research Letters*, *36*, L16302. https://doi.org/10.1029/2009GL039297

Wilson, T. J., Bevis, M., Konfal, S., Barletta, V., Aster, R., Chaput, J., et al. (2015, April). Understanding glacial isostatic adjustment and ice mass change in Antarctica using integrated GPS and seismology observations. In *EGU General Assembly Conference Abstracts*, (Vol. *17*).

Winberry, J. P., & Anandakrishnan, S. (2003). Seismicity and neotectonics of West Antarctica. *Geophysical Research Letters*, *30*(18), 1931. https://doi.org/10.1029/2003GL018001

Winberry, J. P., & Anandakrishnan, S. (2004). Crustal structure of the West Antarctic rift system and Marie Byrd Land hotspot. *Geology*, *32*(11), 977–980. https://doi.org/10.1130/G20768.1

Wobbe, F., Lindeque, A., & Gohl, K. (2014). Anomalous South Pacific lithosphere dynamics derived from new total sediment thickness estimates off the West Antarctic margin. *Global and Planetary Change*, *123*, 139–149. https://doi.org/10.1016/j.gloplacha.2014.09.006

Wu, P., Wang, H., & Steffen, H. (2012). The role of thermal effect on mantle seismic anomalies under Laurentia and Fennoscandia from observations of glacial isostatic adjustment. *Geophysical Journal International*, *192*(1), 7–17. https://doi.org/10.1093/gji/ggs009

Yuan, Y. O., Simons, F. J., & Tromp, J. (2016). Double-difference adjoint seismic tomography. *Geophysical Journal International*, *206*(3), 1599–1618. https://doi.org/10.1093/gji/ggw233

Zhao, D. (2007). Seismic images under 60 hotspots: Search for mantle plumes. *Gondwana Research*, *12*(4), 335–355. https://doi.org/10.1016/j.gr.2007.03.001

Zhao, Y., Liu, X., Song, B., Zhang, Z., Li, J., Yao, Y., & Wang, Y. (1995). Constraints on the stratigraphic age of metasedimentary rocks from the Larsemann Hills, East Antarctica: Possible implications for Neoproterozoic tectonics. *Precambrian Research*, *75*(3-4), 175–188. https://doi.org/10.1016/0301-9268(95)80005-3

Zhou, Y., Dahlen, F. A., & Nolet, G. (2004). Three-dimensional sensitivity kernels for surface wave observables. *Geophysical Journal International*, *158*(1), 142–168. https://doi.org/10.1111/j.1365-246X.2004.02324.x

Zhu, H., Bozdağ, E., & Tromp, J. (2015). Seismic structure of the European upper mantle based on adjoint tomography. *Geophysical Journal International*, *201*(1), 18–52. https://doi.org/10.1093/gji/ggu492

Zhu, H., Komatitsch, D., & Tromp, J. (2017). Radial anisotropy of the north American upper mantle based on adjoint tomography with USArray. *Geophysical Journal International*, *211*(1), 349–377. https://doi.org/10.1093/gji/ggx305